MEMS Structures for Stress Measurements for Thin Films Deposited Using CVD

by

Yu-Hin F. Lau

B.S., Materials Science and Engineering (1998)

Cornell University

Submitted to the Department of Materials Science and Engineering
in partial fulfillment of the requirements for the degree of

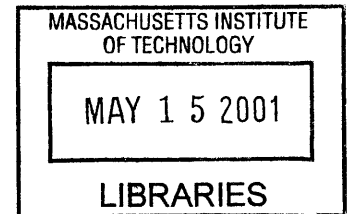Master of Science in Materials Science and Engineering

at the

Massachusetts Institute of Technology

February 2001

Signature of Author...
Department of Materials Science and Engineering
September 12, 2000

Certified by ....
Carl V. Thompson
Stavros Salapatas Professor of Materials Science and Engineering
Thesis Supervisor

Accepted by ....
Carl V. Thompson
Stavros Salapatas Professor of Materials Science and Engineering
Chairman, Departmental Committee on Graduate Students

MEMS Structures for Stress Measurements for Thin Films Deposited Using CVD

by

Yu-Hin F. Lau

B.S., Materials Science and Engineering (1998)
Cornell University

Submitted to the Department of Materials Science and Engineering
on September 12, 2000 in partial fulfillment of the requirements for the degree of
Master of Science in Materials Science and Engineering

ABSTRACT

Mechanical stress in thin films is an important reliability issue in microelectronic devices and systems. The presence of large stresses can lead to the formation of defects that can cause device failure. The ability to control the magnitude of stress during film formation is, therefore, crucial to the fabrication of defect-free and reliable electronic devices and systems. However, the origin of stress in thin films is still a subject of intense debate. The development of a detailed understanding of the origin of stress hinges on our ability to make accurate stress measurements during and after film deposition. To this end, two novel MEMS structures were developed to measure the stress of thin films deposited using chemical vapor deposition (CVD).

Buckled SOI membranes were designed and fabricated for the measurement of the stress in thin films deposited on them. A simple analytic model was developed and calibrated to assess the pre-deposition and post-deposition buckling of the structures. By measuring the changes in mechanical responses upon film deposition, it was successfully demonstrated that stress in thin films can be accurately measured. In particular, the stresses in evaporated chromium films measured using the SOI membranes and the curvature method were found to agree to within 5%.

Stress pointers were designed and fabricated for in-situ stress measurements of CVD thin films. The design was based on mechanically amplified rotation and the novel concept of "footprinting". Stress is recorded during film formation in the form of beam rotation, which is also dependent on film thickness. As a result, stress can be measured as a function of film thickness in post-deposition analyses, without using real-time measurements during deposition. The fabricated structures were found to bend down and stick to the substrate. PECVD films were found to deposit non-uniformly underneath the beams, thereby complicating the mechanical responses of the stress pointers. A new and improved design is proposed.

Thesis Supervisor: Carl V. Thompson
Title: Stavros Salapatas Professor of Materials Science and Engineering

2

Acknowledgements

Numerous people contributed to the completion of this thesis. Professor Carl Thompson, my thesis advisor, offered me continuous guidance and immense freedom to pursue my research in the past two years. He set ambitious goals for my projects and yet trusted fully in my ability to achieve them, thereby providing me many invaluable learning opportunities. I am grateful for everything he did.

I would also like to thank Professor Stephen Senturia for his insights and the many useful discussions we had. His relentless drive for making accurate prediction of the electromechanical responses of MEMS structures had given me many precious lessons that I would not forget.

I am glad to have the opportunity to work alongside members of my research group, who made 13-5143 a cool place to hang out and do productive work. Group lunches and dinners were always filled with laughter because of them. In particular, I want to thank Robert Bernstein, Mauro Kobrinsky, and Steve Seel for their assistance in many aspects of this work. Special thanks must go to Rob, who gave me a tremendous amount of help with mask layout and fabrication. Without his expertise, it would have taken me infinitely longer to achieve what we had accomplished. Erik Deutsch and Alicia Volpecilli in Professor Senturia's group also deserved special recognition. Erik got me off the ground when I first joined the M-Test group. Alicia taught me Visual C++ programming for the automation of M-Test.

Technicians and specialists in the Microsystems Technology Laboratories were helpful in many ways. I would particularly like to thank Kurt Broderick and Paul Tierney, who went above and beyond their call of duty to help students solve their problems. Their professionalism is greatly appreciated.

I also had the good fortune to make friends with many fascinating people in the department – Pat, Huankiat, Justin, Larry, Mel, and Christine, just to name a few. The conversations we had, from career choices to biological warfare, were always fun and inspiring. In particular, I want to express my sincerest gratitude to Pat, Huankiat, and Justin for making my dream come true, by giving birth to *Lorien* – our fictitious dim sum restaurant chain. No matter what they eventually do, I am sure they will all achieve great things that will change the world.

Finally, I would like to thank my parents, Frank and Catherine, my sister Grace, my grandma, and my girlfriend Eve for their untiring love and support. Without their encouragement, especially Eve's 7:30am wake-up call every morning, I would never have made it this far. I love you all.

Contents

List of Figures

7

List of Tables

Chapter 1

Introduction

Integrated circuits (ICs) have completely transformed the way people work and live in the past half century, penetrating virtually every sector from consumer goods to computers and communications. In each IC, there are thousands or even millions of transistors, each acting as a switch that manipulates electronic signals. In 29 years, the number of transistors in a microprocessor (commonly referred to as a chip) has increased more than 12,000 times, from 2300 in the Intel 4004 in 1971 to 28 million in the most recent Intel Pentium III Xeon processor. But the size of a processor has remained unchanged. At the heart of this tremendous progress in miniaturization lies the ability to fabricate reliable and defect-free electronic devices – since one failure can render the entire chip useless – in which materials play a critical role.

To form a transistor, electronic materials are either grown or deposited on silicon wafers in the form of very thin films (usually with thickness less than 1μm) that are patterned into different shapes. A potential consequence of processing bonded dissimilar materials is the generation of *residual stresses*, which commonly arise due to the difference in thermal expansion coefficients (known as thermal stress), lattice mismatch

in heteroepitaxial growth (known as epitaxial stress), and the nucleation and growth processes (known as intrinsic stress). It is well known that, depending on processing conditions, the magnitude of these stresses can vary from a few GPa in compression to a few GPa in tension [Ohr 92]. However, the origin of these stresses is still a subject of intense debate. Even though stress in itself is not considered a defect per se, the presence of large stresses can lead to the formation of defects such as hillocks, stacking faults, cracking, warping, and delamination. Consequently, manufacturing yield and circuit reliability depend heavily on how effectively these stresses are controlled.

Concurrently, the field of micro-electromechanical systems (MEMS) has grown significantly in the last decade. Micron-size machines such as combustion engines, accelerometers, and gyroscopes have been fabricated using on silicon processing technologies developed for IC fabrication, and these MEMS devices have found increased commercial use. Stress has also been found to be an important reliability issue for MEMS. For example, large out-of-plane bending can occur in free-standing beams if the structural material has a through-thickness stress gradient. It has also been found that a small compressive stress in micro-machined polysilicon structures can lead to buckling in doubly-supported beams and render them non-functional [Kob 00]. To design micro-machines with optimal electromechanical responses, precise control of the *elastic properties* of the materials that constitute these machines is also essential. However, most technologically important thin films, unlike bulk materials, exhibit preferential crystallographic orientation, resulting in anisotropic elastic properties that can vary substantially with processing conditions. [Tho 93]

Without doubt, a full understanding of nucleation and growth processes and their dependence on processing conditions is necessary for the production of films with well-controlled stress and elastic properties. Whether this can be accomplished hinges on our

ability to make accurate and sensitive measurements of these material properties *during* film formation and subsequent processing at elevated temperatures. However, mechanical testing of thin films is a difficult and complex problem in itself, because of the small size scale. It is, therefore, not surprising that reported values for the Young's modulus of polycrystalline silicon films vary over a wide range, from 90 to 190 GPa [Sch 92]. This discrepancy can be attributed to the different processing conditions used for the films studied and, just as importantly, the inadequacy of the measurement techniques themselves. Building upon past research, this thesis is an attempt to propose new methodologies for the measurement of stress and elastic properties of thin films formed by one of the common deposition methods, *chemical vapor deposition.*

1.1   Thin Film Deposition

Thin film deposition is the process of transferring atoms from a material source to a substrate, where electronic devices are built using materials with the desired composition and properties. There are three main types of deposition in microelectronic fabrication – electrodeposition, physical vapor deposition (PVD) and chemical vapor deposition (CVD).

Electrodeposition is primarily used in copper metallization. In contrast with most deposition methods, electrodeposition takes place in a plating solution instead of a vacuum system. To form a film, copper ions are transported from a positively charged copper source to a negatively charged substrate, which is usually covered with a copper seed layer deposited by other means. The ions are then deposited on the surface of the

15

substrate in the form of atoms. Deep trenches can be filled with relative ease using this method.

In PVD, atoms are physically transferred from the source to the substrate either by evaporation or sputtering. Evaporation is typically performed in a high vacuum, with base pressures from 10^{-7} to 10^{-9} torr. The source is caused to evaporate through heating with an electron beam until, for example, a sufficiently high vapor pressure is achieved. The evaporated atoms then travel in a straight line to the substrate and condense to form a film. On the other hand, sputtering is generally performed in an Argon atmosphere, with gas pressures ranging from a few to 100 mtorr. Sputtering is caused by bombardment of a source with highly energetic ions that physically remove the target source atoms. The dislodged atoms undergo many collisions with gas particles before they eventually deposit on the substrate, making the deposition less susceptible to physical shadowing. As a result, sputtered films generally have better step coverage than evaporated films. In addition, sputter deposition usually allow for more variations in composition than evaporative deposition because it is possible to sputter multi-component targets with a fixed stoichiometry of the sputtered material.

CVD films are usually formed from reactive gases that are introduced onto the surface of the substrate. The films normally have superb uniformity and step coverage. CVD also has the ability to produce a large variety of films of metals, semiconductors, and compounds with different stoichiometries, in either amorphous or crystalline form, since the gas chemistry can be altered fairly easily. In commercial applications, CVD is usually preferred over PVD because it allows for batch processing and has faster deposition rates, resulting in higher throughput. It is important to note that CVD films generally cover all the exposed surfaces on a wafer because they deposit wherever the

gases can penetrate. This is an important distinction that directly affects the design of stress measurement tools, as we shall see later in the chapter.

1.2   Stress Measurement Techniques

Perhaps the earliest and most widely adopted technique for measuring stress in thin films is through wafer curvature measurements. The theory behind this technique is based on the original work on electroplated beams by Stoney in 1909, which was later extended to include plates by Hoffman in 1966 [Glo 95]. Before any film is deposited, the radius of curvature of a bare wafer is first measured. In a typical stress measurement system, this is done by scanning a laser beam across a wafer using a rotating mirror. The angle of reflection, θ, is measured as a function of position, x, with a light detector. A schematic illustration is shown in Figure 1-1 [Tencor]. The average radius, calculated by performing linear regression, is the rate of change of θ with respect to x. After the film is deposited, the stress in the film exerts a bending moment on the wafer and changes the radius of curvature. The change is related to the film stress by what is now known as
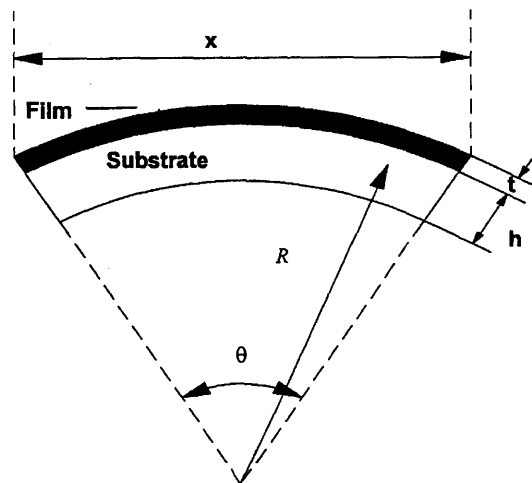
Figure 1-1. Schematic of the wafer curvature method. [Tencor]

17

Stoney's equation, which is given by

$$\sigma = \frac{E}{6(1-\upsilon)} \frac{h^2}{t} \left(\frac{1}{R_{after}} - \frac{1}{R_{before}} \right)$$ (1.1)

where $E/1-\upsilon$ is the biaxial modulus of the wafer.

The curvature method is a relatively simple way to measure the residual stress in as-deposited films, as well as the change in film stress during annealing [Kus 98, Kob$_2$ 00, Win 00]. It has also been used to measure stress in-situ during molecular beam epitaxy (MBE) growth of silicon-germanium and boron films using a multi-beam optical sensing technique to detect the change in curvature [Flo 97, Nes 99]. Despite its wide applications, there are still some limitations to use of the curvature method. First, films are required to be deposited on one side of the wafer only, or the curvature will remain unchanged because of moment-balancing. CVD will form films on the backside of wafers, which have to be etched away before measurements can be made. This makes the curvature method unsuitable for in-situ use in CVD systems. Furthermore, for a given stress, the amount of wafer bending decreases as the square of the wafer thickness. Consequently, the ability to measure small stresses in thin films decreases when larger wafers with greater thicknesses are used.

The main source of error in the curvature method is the replacement accuracy of wafers. The placements of the wafers, when measurements are made for the second time, are unavoidably different, even though only slightly, from those made before films are deposited. This gives rise to errors since wafers seldom have the perfect shape of a spherical cap. For a substrate thickness of 290µm, the sensitivity of the curvature method has been found to be on the order of a few MPa-µm. (The stress-thickness product, MPa-

18

μm, is commonly used as a figure of merit to quantify the sensitivity of stress measurement techniques. A sensitivity of 1MPa-μm means the smallest detectable stress is 1MPa for a 1μm thick film, and 10MPa for a 0.1μm thick film.)

Techniques based on the surface analysis of materials, such as ones using Raman spectroscopy [Ben 95], Fourier transform infrared spectroscopy [Sam 92], and X-ray [Kus 96], have also been investigated as potential in-situ stress monitoring tools, albeit with only moderate success. These techniques require a number of simplifying assumptions about the texture, microstructure and defect density of the film, as well as the interaction between the film and the incident phonons. These assumptions are seldom accurate enough for quantitative measurement of actual thin films. These techniques also require a long sampling time to collect a strong enough signal for analysis. The capability for in-situ stress measurement, as a result, is difficult to achieve.

1.3   The MEMS Approach

With the development of surface micromachining has come a new generation of techniques and novel devices. Figure 1-2 shows some examples of MEMS structures that are built for mechanical property measurements. MEMS techniques have three major advantages over the curvature method. First, measurements can be performed in a very local area on a wafer due to the small size of MEMS devices. Information on the uniformity of the deposition process can thus be obtained. Second, these techniques have the potential to be used on-chip because they are closely compatible with silicon processing technologies. Hence, mechanical properties of thin films can be measured real-time by tiny sensors on a wafer during manufacturing. Third, MEMS devices can be

made to be sensitive to small changes in stress and elastic properties regardless of the wafer thickness because they are usually thin, with thicknesses on the order of 1-2μm.

So far, these potentials have only been realized for films deposited by evaporative and sputtered deposition, for which an array of techniques have been developed. Among them, two have received the most interest – the bending of cantilever beams [Klo 68, Abe 90, Kim 99] and the electrostatic pull-in of cantilevers, doubly-supported beams, and circular diaphragms [Ost 97, Bla 98]. In both techniques, the film under investigation is deposited on fabricated MEMS structures and the change in deflection (for beam bending) or pull-in voltage (for electrostatic pull-in) is measured to extract material properties. These two techniques, however, are not suitable for use in CVD systems. In the case of beam bending, films can cover both sides of the beam, resulting in a stress-balanced and unbent beam. In the case of electrostatic pull-in, films can deposit between the beams and the electrodes, thereby shorting (for metal film) or insulating (for dielectric film) the electrical circuit elements that apply the bias and detect pull-in.

Only ex-situ MEMS techniques have been proposed for CVD films. Some

| (a) | (b) | (c) |
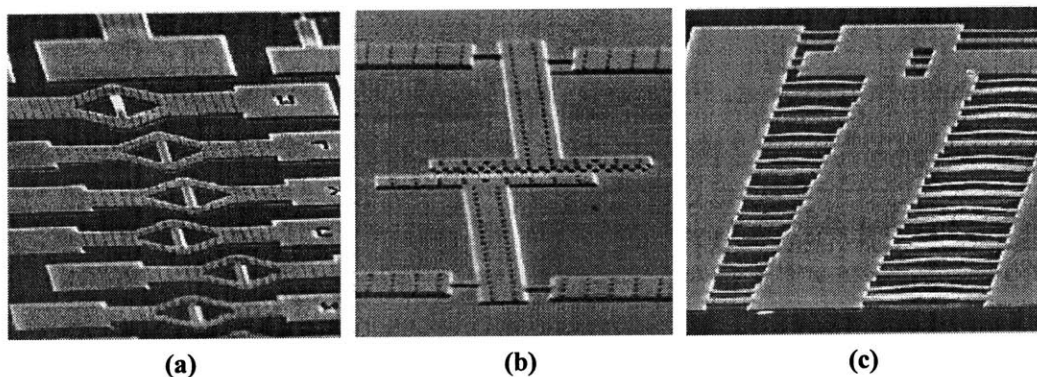
Figure 1-2. SEM photographs of some examples of MEMS structures for material property extraction – **(a)** a series of diamond structures for the measurement of tensile stresses, **(b)** a single set of rotating beam structures for the measurement of both tensile and compressive stresses, **(c)** and an array of buckled microbridges for the measurement of compressive stresses. [Elb 97]

examples include the bulge test of clamped square membranes [Vla 92], the uniaxial tension test of opposing microfabricated structures with different widths [Meh 87], and the bent-beam technique using rotating polysilicon structures [Gia 96]. The majority of these MEMS-based techniques employ the methodology that the film under investigation is patterned into the desired mechanical structures, from which measurements are made. This poses a number of restrictions and limitations. First, changes in the mechanical properties of the as-deposited film that occur immediately after deposition – which can result from oxidation, room temperature recrystallization, and stress relaxation – are not detected as the film has to go through further processing. In addition, films that are much thicker than those used in actual electronic devices are often tested because thinner films are less likely to survive the measurement process. There is also little flexibility in the choice of the substrate material on which the film is deposited, even though it is well known that the substrate plays an important role in the initial phase of film formation and in epitaxial growth. Polysilicon films, for instance, are predominantly deposited on sacrificial silicon dioxide layers.

1.4   Thesis Organization

CVD films are one of the most technologically important and relevant materials. And yet, there is a lack of reliable methods for the characterization of their mechanical properties during and after film deposition. It is therefore the goal of this thesis to investigate new methodologies, based on the MEMS approach, for the ex-situ and in-situ measurement of the stress of CVD films.

In the previous section, it is noted that there is no net bending in a MEMS structure when it is covered on all sides with a deposited film. Although the structure is stress-balanced, there is still a very small and difficult to measure in-plane strain due to the residual stress. Potentially, the stress can be extracted if the in-plane strain is converted into some measurable quantities. Chapter 2 presents a method that makes use of the buckling of SOI membranes to translate small in-plane strain into relatively large and measurable deformations, which is related to the residual stress in the film and can be measured in ex-situ experiments.

Real-time measurement tools often require special setups which are difficult to accomplish in commercial batch processing equipment. Chapter 3 describes a rotation technique that magnifies in-plane strain into relatively large lateral displacements. The displacements are modulated by a film thickness dependent stopping mechanism that records the history of stress evolution during deposition. In this way, "in-situ" measurements are performed after deposition without the need for real-time measurement tools. Chapter 4 then summarizes the work presented and suggests future work.

Chapter 2

Ex-Situ Technique: *SOI Membranes*

2.1   Introduction

When a perfectly straight beam is compressed, its straight form is initially in a stable equilibrium, meaning that the beam remains straight even if it is perturbed. As the load gradually increases, a critical point is reached when a slight perturbation produces a stable lateral deflection. This phenomenon is referred to as buckling. The critical load for buckling, P_{cr}, can be solved using a differential equation describing a deflected beam. The case of a beam with one end fixed and the other end axially loaded was first discussed by Euler [Tim 36], the solution of which was given by

$$P_{cr} = \frac{\pi^2 EI}{4\ell^2}, \tag{2.1}$$

where ℓ is the length of the beam, E is the Young's modulus, and I is the moment of inertia of the beam. Buckled beams typically have deflections that are relatively large and measurable, thereby forming a useful basis for measuring the compressive stress in

the beam. In this chapter, we will describe the design and fabrication of silicon-on-insulator (SOI) membranes, on which thin films can be deposited. Changes in the buckling behavior of these membranes are then used to characterize the stress of the film.

The use of buckling in residual stress measurement was first applied to MEMS by Guckel et al. using an array of clamped polysilicon beams with different lengths [Guc 85]. While the longer beams buckled, the shorter ones remained straight. To measure the compressive stress, the critical buckling length – the length of the shortest buckled beam – was determined by visually examining the beams using an electron microscope. Later, a more novel structure that was shaped like a diamond was proposed to characterize the residual stress in tensile films [Guc 92]. Since then, more sophisticated analytic models have been developed to include effects such as structural imperfection [Fan 94] and non-linearity [Nic 99] in beams. In addition to beams, the buckling of square membranes has also been studied to measure the residual stress in compressive films [Pop 94, Zie 99]. Generally, the film under investigation is patterned into the desired structures – either beams or membranes – and the magnitude of deflection is measured. As a result, the film must be under compressive stress, or no buckling will occur. Furthermore, in the case of beams, there must be a reliable process to pattern the film into the desired shapes. Therefore, copper films, for which there is a lack of a dry etching technique, are not suitable for the above techniques. In the case of membranes, the film must be resistant to chemical etchants,, such as potassium hydroxide (KOH) and tetramethylammonium hydroxide (TMAH) solutions, that are used during backside etching. These requirements have imposed significant limitations on the use of these devices.

2.2　　　Sensor Design and Device Layout

The difficulties mentioned above can be overcome by depositing the film of interest on buckled membranes. The stress of the film changes the magnitude of deflections of the membranes. The film no longer needs to be patterned nor to be in contact with etching solutions. In addition, both tensile and compressive stresses can be measured.

The silicon-on-insulator (SOI) membranes used in this work are composed of a 2μm-thick single crystal silicon layers with a 2μm-thick thermally grown silicon dioxide layers underneath. They are fabricated from SOI wafers by anisotropically etching the backsides, resulting in sloped backside cavities. There are 23 membranes in various sizes on a 1cm × 1cm die as shown in Figure 2-1. Table 2-1 lists the dimensions of the openings in the photo mask and the resulting sizes of the membranes. The membrane sizes are calculated assuming that the (111) planes are the planes with the slowest etch rate and that the wafer is 450μm thick. In order to measure both compressive and tensile stresses, the membranes are designed to buckle even without film deposition. This is
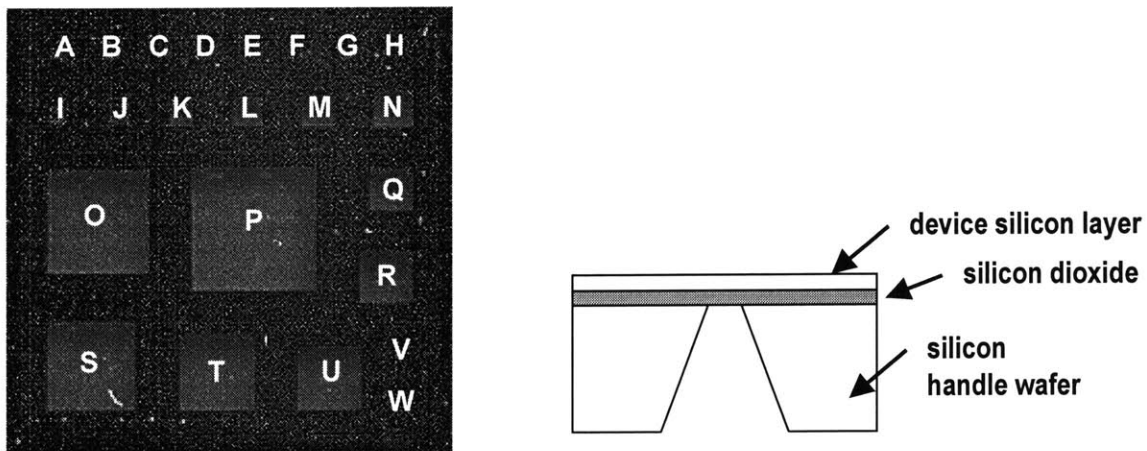
Figure 2-1. Front view of a die, 1cm × 1cm in size, with processed square membrane structures. The labels correspond to the names used in Table 2-1. A cross-sectional view of a membrane is shown on the right.

Table 2-1. Dimensions of the backside openings laid out on the photo mask and the resulting membrane sizes. Labels for the membranes are shown in Figure 2-1. The sizes of the membranes are calculated assuming a wafer thickness of 450μm.

Membrane	Backside	Calculated Size	Membrane	Backside	Calculated Size
V	686	50	K	1036	400
W	686	50	L	1136	500
H	711	75	M	1236	600
G	736	100	N	1336	700
F	761	125	Q	1436	800
E	786	150	R	1636	1000
D	811	175	U	1886	1250
C	836	200	T	2136	1500
B	861	225	S	2386	1750
A	886	250	O	2636	2000
I	936	300	P	3136	2500
J	986	350	All values listed in μm.		

accomplished because the silicon dioxide layers are under compressive stress. Most membranes buckle in the first buckling mode, the shape of which resembles a cone. Films can be deposited on either one side or both sides of the membranes because buckling is determined by the in-plane stress, not the moment, in the membranes. So, even though the membranes are moment-balanced when films are deposited on both sides, the in-plane stress is in fact twice as much as when films are deposited on one side only. Changes in the buckling behavior due to the additional film, which can be deposited either before or after the release of the membranes, are then used to extract the residual stress of the film.

The mechanical responses of these membranes are rather complex because of bending-stretching coupling that is characteristic of unsymmetric laminated plates, defined as plates that are asymmetric with respect to the middle plane of the plate. The analytical solutions for this type of membrane generally require finite element simulations or numerical solutions [Jen 88, Qat 93]. This approach, however, is not practical for material property extraction as the number of parameters are too numerous and the resulting expression will be too cumbersome to use. By restricting the analysis to

first mode buckling and utilizing the Rayleigh-Ritz energy method, a simple analytic model for the extraction of mechanical properties is developed and presented in the next section.

2.3 Analytic Model

2.3.1 Approximate Buckling Solution for Clamped, Square Laminated Plates

In large deflection theory, when the out-of-plane deflection is comparable to the thickness of the plate, the buckling response is non-linear. The governing differential equations for such a case generally do not yield closed-form solutions. Hence, the Rayleigh-Ritz energy method [Tim 36], on which this analysis is based, is typically used to obtain an approximate solution by minimizing the elastic strain energy of the plate.

We first consider a square laminated plate of size 'a' with rigidly clamped edges. The center of this plate is situated at the origin of a Cartesian coordinate system. The reference surface, $z=0$, is taken at the neutral plane, where the top surface of the laminate is located at $z=h_2$ while the bottom surface is at $z=-h_1$. The plate is composed of an arbitrary number of anisotropic and homogeneous layers, each with different elastic stiffness constants $c_{ij}^{(k)}$, residual strain $\varepsilon_0^{(k)}$, and thickness $h^{(k)}$, where the superscript k denotes the kth layer of the composite plate.

27

For a thin plate with thickness much less than all its other dimensions, it is assumed to be in a state of plane stress and all stresses, except σ_x, σ_y, and σ_{xy}, are zero. The elastic strain energy for such a plate is given by

$$U = \frac{1}{2} \iiint\limits_{vol.} \left(\sigma_x \varepsilon_x + \sigma_y \varepsilon_y + \sigma_{xy} \varepsilon_{xy} \right) dV, \qquad (2.2)$$

where ε_x and ε_y are normal strains, and ε_{xy} is the shear strain; σ_x and σ_y are normal stresses, and σ_{xy} is the shear stress. The stress-strain relationships of thin laminated plates, unlike those of thin homogeneous plates, have to satisfy interfacial continuity conditions in addition to the equilibrium conditions for each layer. The complete solution was presented by Lekhnitskii and later extended to a more general case by Ambartsumyan [Bog 96]. The resulting plane-stress constitutive equation, for the kth layer in a laminated plate, is given by [Whi 87]

$$\begin{bmatrix} \sigma_x^{(k)} \\ \sigma_y^{(k)} \\ \sigma_{xy}^{(k)} \end{bmatrix} = \begin{bmatrix} Q_{11}^{(k)} & Q_{12}^{(k)} & Q_{16}^{(k)} \\ Q_{12}^{(k)} & Q_{22}^{(k)} & Q_{26}^{(k)} \\ Q_{16}^{(k)} & Q_{26}^{(k)} & Q_{66}^{(k)} \end{bmatrix} \begin{bmatrix} \varepsilon_x^{(k)} \\ \varepsilon_y^{(k)} \\ \varepsilon_{xy}^{(k)} \end{bmatrix}, \qquad (2.3)$$

where the reduced stiffness terms Q_{ij} are related to the elastic stiffness constants, c_{ij}, as

$$Q_{ij} = c_{ij} - \frac{c_{i3} c_{j3}}{c_{33}}. \qquad (2.4)$$

Knowing that the deformation results in small strains but large deflections, the von Kármán's non-linear strain-displacement relations are used, where, for the kth layer, we have [Chi 80]

$$
\begin{bmatrix} \varepsilon_x^{(k)} \\[4pt] \varepsilon_y^{(k)} \\[4pt] \varepsilon_{xy}^{(k)} \end{bmatrix} = \begin{bmatrix} \varepsilon_0^{(k)} \\[4pt] \varepsilon_0^{(k)} \\[4pt] {} \end{bmatrix} + \begin{bmatrix} \dfrac{\partial u}{\partial x} \\[8pt] \dfrac{\partial v}{\partial y} \\[8pt] \dfrac{\partial u}{\partial y} + \dfrac{\partial v}{\partial x} \end{bmatrix} + \begin{bmatrix} \dfrac{1}{2}\left(\dfrac{\partial w}{\partial x}\right)^2 \\[10pt] \dfrac{1}{2}\left(\dfrac{\partial w}{\partial y}\right)^2 \\[10pt] \dfrac{\partial w}{\partial x} \cdot \dfrac{\partial w}{\partial y} \end{bmatrix} - z \begin{bmatrix} \dfrac{\partial^2 w}{\partial x^2} \\[8pt] \dfrac{\partial^2 w}{\partial y^2} \\[8pt] 2\dfrac{\partial^2 w}{\partial x \partial y} \end{bmatrix}, \tag{2.5}
$$

where z is the distance from the neutral plane; and w(x,y), u_x(x,y), and u_y(x,y) are the displacement functions for the out-of-plane deflection and the in-plane displacements in the x and y directions, respectively. The first column in equation (2.5) represents the biaxial residual strain of each layer. The second column represents the normal strain caused by any in-plane deformation. The third column is the rotational strain due to large deflection. The contribution of rotational strain does not become significant until the deflection is on the order of the plate thickness and is, therefore, normally neglected in small deflection analyses. The fourth column shows the strain induced by an applied curvature. This portion of the strain becomes zero at the neutral plane.

Here, we further restrict our analysis to cubic and isotropic materials, thus reducing the stiffness matrix to three independent variables – Q_{11}, Q_{12}, and Q_{44} (which is equivalent to Q_{66}) – for cubic materials, and two independent variables – Q_{11} and Q_{12} – for isotropic materials.

To find the strains in equation (2.5), the three displacement functions, w(x,y), u_x(x,y), and u_y(x,y), must be known. For w(x,y), the shape of the deflection surface can generally be written in terms of an infinite sum of some suitably chosen trigonometric functions that satisfy the boundary conditions of a clamped plate:

$$
w(x,y) = \frac{\partial w(x,y)}{\partial x} = \frac{\partial w(x,y)}{\partial y} = 0 \tag{2.6}
$$
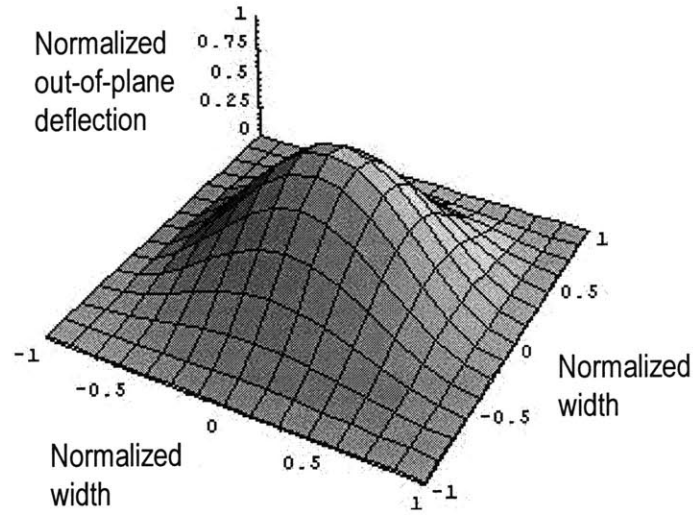
Figure 2-2. The approximated shape of a membrane in the first buckling mode.

at the four edges of the plate. For simplicity, we shall limit the scope of this analysis to the first buckling mode, in which case the shape of a buckled membrane can be approximated in the form of

$$w(x,y) = \frac{w_{max}}{4}\left(1 + \cos\frac{2\pi x}{a}\right)\left(1 + \cos\frac{2\pi y}{a}\right), \tag{2.7}$$

where w_{max} is the maximum deflection, found at the center of the plate. The shape of such a surface is shown in Figure 2-2. The trial functions for the in-plane displacements, on the other hand, must satisfy the boundary conditions:

$$u_x(x,y) = u_y(x,y) = \frac{\partial u_x(x,y)}{\partial y} = \frac{\partial u_y(x,y)}{\partial x} = 0 \tag{2.8}$$

at the four edges. In addition, they must be compatible with equation (2.7) since the out-of-plane deflection defines the in-plane displacements. Consequently, the trial functions can be written as

30

$$\begin{cases} u_x(x,y) = c \sin\dfrac{2\pi x}{a}\left(1 + \cos\dfrac{2\pi y}{a}\right) \\[2mm] u_y(x,y) = c \sin\dfrac{2\pi y}{a}\left(1 + \cos\dfrac{2\pi x}{a}\right) \end{cases} \tag{2.9}$$

for the displacement in the x and y directions, respectively, where c is a variable.

Evaluating equation (2.2) and utilizing the fact that residual stress and elastic properties are constant within a homogeneous layer, we have, for a laminated plate with n layers, the expression for the elastic strain energy, U:

$$\begin{aligned}
U = \ & (A_{12} - A_{44})\frac{\pi^3 c w_{max}^2}{4a} + (21A_{11} + 5A_{12} + 10A_{44})\frac{5\pi^4 w_{max}^4}{4096a^2} \\
& + (3A_{11} + A_{12} + 2A_{44})c^2\pi^2 + (3B_{11} + B_{12} + 2B_{44})\frac{\pi^3 c w_{max}}{2a} \\
& + (B_{12} - B_{44})\frac{\pi^4 w_{max}^3}{8a^2} + (3D_{11} + D_{12} + 2D_{44})\frac{\pi^4 w_{max}^2}{4a^2} \\
& + \frac{3\pi^2 w_{max}^2}{16}\cdot\sum_{k=1}^{n} h^{(k)}\sigma_o^{(k)}
\end{aligned} \tag{2.10}$$

where

$$(A_{ij}, B_{ij}, D_{ij}) = \int_{-h_1}^{h_2} Q_{ij}^{(k)}(1,z,z^2)\,dz \tag{2.11}$$

and $\sigma_o^{(k)}$ is the residual stress of the kth layer. In this form, the integrals are evaluated with respect to the common neutral plane at z=0. To take advantage of the symmetry about the middle plane of each layer, we transform the axes [Tsa 88] such that the integrals are evaluated with respect to the middle plane of each individual layer, as illustrated in Figure 2-3. Equation (2.11) then becomes

31

$$\begin{cases} A_{ij} = \sum_{k=1}^{n} Q_{ij}^{(k)} h^{(k)} \\ B_{ij} = \sum_{k=1}^{n} A_{ij}^{(k)} d^{(k)} \\ D_{ij} = \sum_{k=1}^{n} A_{ij}^{(k)} \left(d^{(k)2} + \frac{1}{12} h^{(k)2} \right) \end{cases} . \tag{2.12}$$

The transformation results in the quantity $d^{(k)}$, which is the distance between the middle plane of the kth layer and the common neutral plane of the laminated plate. The neutral plane is defined as the plane where the strain due to an applied curvature vanishes. For isotropic or mid-plane symmetric plates, the neutral plane coincides with the middle plane of the entire laminate. However, for unsymmetric plates, it can be shown, using a force balance analysis (see Appendix A), that the location of the neutral plane can be found by satisfying the condition:

$$B_{11} + B_{12} = 0. \tag{2.13}$$

The minimum in the elastic strain energy of the plate is then found by solving the two equations,

$$d = z_{\substack{middle \\ plane}} - z_{\substack{common \\ neutral \ plane}}$$
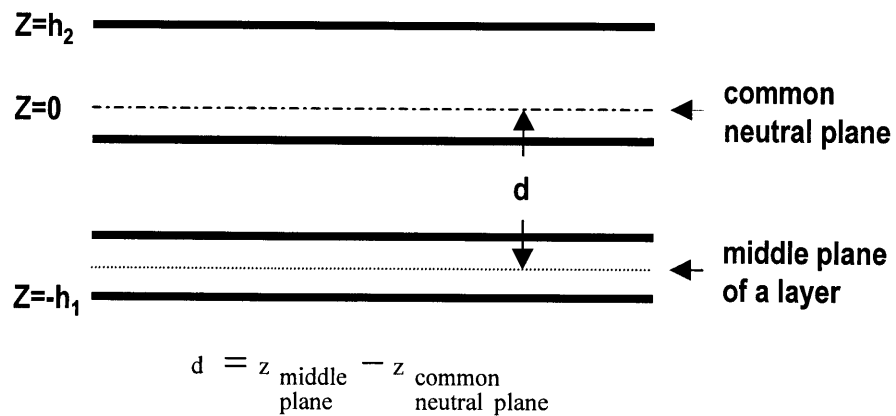
Figure 2-3. Schematic illustration showing the transformation of axes in an imaginary three-layered laminate. The distance between the middle plane of a layer and the common neutral plane, d, is given by the equation in the figure.

$$\frac{\partial U}{\partial w_{max}} = 0 \qquad \frac{\partial U}{\partial c} = 0 , \qquad\qquad (2.14)$$

which gives the solutions

$$\begin{cases} w_{max}^{flat} &= \quad 0 \\ w_{max}^{up} &= \quad \beta_1 + \sqrt{\beta_1^2 - \beta_2 - \beta_3 Sa^2} , \\ w_{max}^{down} &= \quad \beta_1 - \sqrt{\beta_1^2 - \beta_2 - \beta_3 Sa^2} \end{cases} \qquad (2.15)$$

where

$$\begin{cases} \beta_1 = \dfrac{192\left[(A_{12} - A_{44})(3B_{11} + B_{12} + 2B_{44}) - (B_{12} - B_{44})(3A_{11} + A_{12} + 2A_{44})\right]}{5(21A_{11} + 5A_{12} + 10A_{44})(3A_{11} + A_{12} + 2A_{44}) - 64(A_{12} - A_{44})^2} \\[4mm] \beta_2 = \dfrac{512\left[(3A_{11} + A_{12} + 2A_{44})(3D_{11} + D_{12} + 2D_{44}) - (3B_{11} + B_{12} + 2B_{44})^2\right]}{5(21A_{11} + 5A_{12} + 10A_{44})(3A_{11} + A_{12} + 2A_{44}) - 64(A_{12} - A_{44})^2} \\[4mm] \beta_3 = \dfrac{384(3A_{11} + A_{12} + 2A_{44})}{5\pi^2(21A_{11} + 5A_{12} + 10A_{44})(3A_{11} + A_{12} + 2A_{44}) - 64\pi^2(A_{12} - A_{44})^2} \\[4mm] S = \displaystyle\sum_{k=1}^{n} h^{(k)}\sigma_0^{(k)} \end{cases} \qquad (2.16)$$

The solution $w_{max}=0$ corresponds to the flat state. This is the only solution when the applied stress is below the critical buckling load. The other two solutions are imaginary. Above the critical buckling load, the positive solution represents the buckled-up state while the negative solution represents the buckled-down state. The two states are slightly different in magnitude because of the terms B_{ij}'s, which have finite values for unsymmetric laminated plates. In the cases of isotropic and symmetric laminated plates, the terms B_{ij}'s vanish and the two solutions become identical in magnitude. The strain energies are slightly different for the two states. One of the states, as a result, will be energetically more favorable than the other. It can also be seen that the clamped-edge boundary condition averages the through-thickness stress gradient, resulting in a thickness-averaged stress quantity.

For comparison, the solution is recast into the form used by Ziebart et al. [Zie 99] for isotropic plates as

$$\frac{w_{max}}{h} = \sqrt{-\frac{192(1+\upsilon)}{65\pi^2}\left(\frac{4.386}{1+\upsilon}+\frac{a^2}{h^2}\frac{\sigma_o(1-\upsilon)}{E}\right)}, \qquad (2.17)$$

where $E/1-\upsilon$ is the biaxial modulus. Figure 2-4 shows a comparison of equation (2.17) and the solution in [Zie 99], obtained by performing over 1,000 numerical simulations. The difference between the two solutions is less than 9% over the entire range considered.

2.3.2   Material Property Extraction

Experimentally, the three quantities, β_1, β_2, and $\beta_3 S$ can be obtained by measuring w_{max} as a function of the membrane size 'a' in both the buckled-up and buckled-down states, using the following expressions:
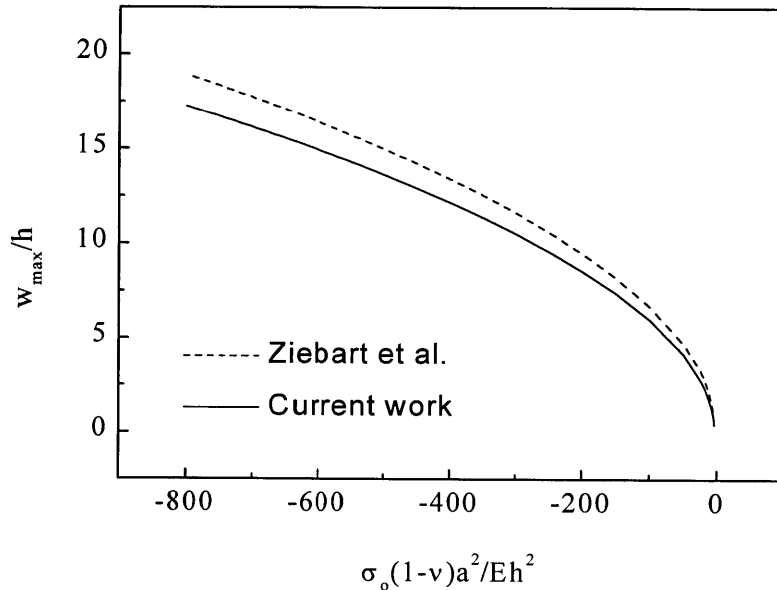
Figure 2-4. Comparison of the approximate solution in the current work for the case of isotropic plates and that obtained by Ziebart et al. [Zie 99] using data from over 1,000 numerical calculations. The difference is less than 9% over the entire range considered.

34

$$\begin{cases} \beta_1 & = & \left(w_{max}^{up} + w_{max}^{down} \right) \Big/ 2 \\ \beta_2 & = & \left(w_{max}^{up} \cdot w_{max}^{down} \right) \quad \text{at} \quad a = 0. \\ \beta_3 S & = & d\left(w_{max}^{up} \cdot w_{max}^{down} \right) \Big/ d\left(a^2 \right) \end{cases} \qquad (2.18)$$

Having three equations relating film properties to experimental measurements, a maximum of three unknown properties – such as residual stress, elastic constants, and film thickness – can be solved in any multi-layer system. However, two challenges remain. First, the prediction of the material properties of the deposited film requires accurate knowledge of the residual stress, elastic properties, and thicknesses of the starting materials, which is not readily available and can vary substantially with processing conditions. Second, the solution presented above is, after all, an approximation. Generally, approximate solutions contain all the correct functional dependence, thereby providing useful insights to otherwise unsolvable problems. However, the level of quantitative agreement attained is seldom satisfactory, as evidenced in the comparison in Figure 2-4. This is a common difficulty encountered by workers in the MEMS area. To overcome this problem, data obtained from finite element modeling of the corresponding MEMS structure are typically used to compare with the approximate solution and the coefficients in the analytic expression are fine tuned. An example of this technique is demonstrated in [Mas 88]. An alternative, and perhaps more practical, approach is to carry out calibration with real device structures and fit the calibration data to the approximate solution to extract the correct coefficients, as outlined in greater detail in the next section.

2.3.3   Device Calibration

To effectively calibrate the mechanical responses of the membranes, it is important to apply a known stress to the structures and then measure the change in out-

of-plane deflections. For the particular design in this work, calibration can be done by heating due to the difference in thermal expansion between silicon and silicon dioxide. Consequently, we have the ability to vary S, relative to the initial residual stress, and a^2 in equation (2.15), to find the coefficient β_3 and the residual stress S, which are given by

$$
\begin{cases}
\beta_3 = \dfrac{d\left[\left(w_{max}^{up/down} - \beta_1\right)^2\right]}{d\left(Sa^2\right)} \\[2ex]
S = \dfrac{1}{\beta_3} \cdot \dfrac{d\left[\left(w_{max}^{up/down} - \beta_1\right)^2\right]}{d\left(a^2\right)}
\end{cases}
, \tag{2.19}
$$

where up/down means that only data that are taken from either all in the up states, or all in the down states are considered. Using thermal expansion data reported by Blech et al. [Ble 82], the change in stress is related to temperature change as

$$
\frac{dS}{dT} = \frac{E_{SiO_2} h_{SiO_2} \left(\alpha_{Si} - \alpha_{SiO_2}\right)}{1 - \upsilon_{SiO_2}} = 0.165 h_{SiO_2} \, MPa - \mu m °C^{-1}, \tag{2.20}
$$

where α_{Si} and α_{SiO_2} are the thermal expansion coefficients of silicon and silicon dioxide, respectively. Applying a thin film approximation, thus assuming the stiffness of the laminated plate does not change with the addition of a film, the stress-thickness product of the deposited film, $h_f \sigma_f$, can be written as

$$
h_f \sigma_f = S_{\substack{with \\ film}} - S_{\substack{without \\ film}} \tag{2.21}
$$

36

2.4   Experiment

2.4.1   Fabrication

The fabrication process for the SOI membranes is shown in Figure 2-5. To fabricate the SOI wafer substrate, 2μm-thick films of silicon dioxide were thermally grown on 450μm thick (100) silicon handle wafers. These were then fusion bonded to (100) silicon device wafers, which were subsequently etched and polished to a nominal thickness of 2μm. Next, the silicon dioxide films grown on the handle wafers were
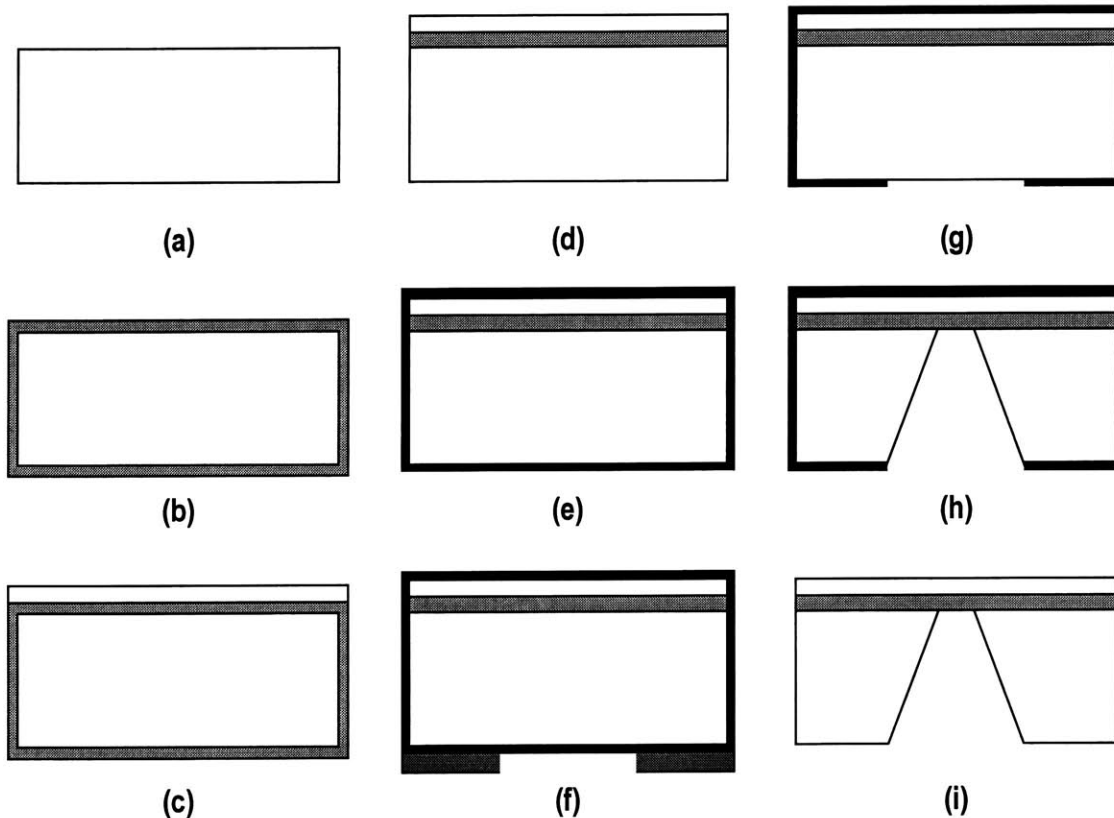
Figure 2-5. The process flow for the fabrication of the SOI membranes – **(a)** (100) silicon handle wafer; **(b)** 2μm-thick thermal oxide; **(c)** wafer bonding with another (100) silicon wafer that is subsequently thinned to a nominal thickness of 2μm; **(d)** removal of the thermal oxide from the backside; **(e)** 1000Å-thick LPCVD silicon nitride; **(f)** patterned photoresist used as etch mask for silicon nitride patterning; **(g)** silicon nitride dry etched; **(h)** backside anisotropic etch using KOH and TMAH; **(i)** silicon nitride stripped using phosphoric acid.

removed from the backsides using a buffered oxide etch, leaving behind layers of silicon dioxide sandwiched between pairs of silicon wafers. The backsides of the bonded wafers were then polished and the wafers were thinned to a final thickness of 434μm. Blanket films of silicon nitride were deposited on both sides of the wafers by low pressure chemical vapor deposition (LPCVD) to function as etch masks. Square openings of various sizes, with edges parallel to the <110> directions of the device layers, were patterned on the backside using reactive ion etching. After the patterning step, the wafers were placed in special Teflon holders in which the front sides of the wafers were protected from wet chemical etching using ethylene propylene (EPR) O-rings while the backsides were exposed to the etch. The wafers were then dipped in 50:1 HF solutions to remove native surface oxide layers. After a quick rinse using de-ionized water, wafers were anisotropically etched in 20wt.% KOH solutions at 85°C until about 60μm of the silicon handle wafers were left. The remaining silicon was etched in 25wt.% TMAH solutions at 85°C with silicon dioxide layers serving as the etch stops. To remove the silicon nitride hard mask, the full wafers were etched in phosphoric acid for 40 minutes at 155°C. The wafers were then diced into 1cm by 1cm dies and the structures were ready for thin film deposition after the magnitude of deflections had been measured.

2.4.2   Device Characterization and Calibration

The vertical profiles of the buckled membranes were measured using a Wyko NT2000 3D optical profiler that had a 0.01μm vertical resolution and a repeatability of better than 0.5%. Measurements were made by passing white light through a beam splitter, with one beam being directed towards the sample and the other being reflected to a reference mirror. Interference fringes, the brightest of which was located at best focus, were generated by combining the light reflected off from the two surfaces. The surface of the sample was scanned along a normal axis, using a piezoelectric motor, and the
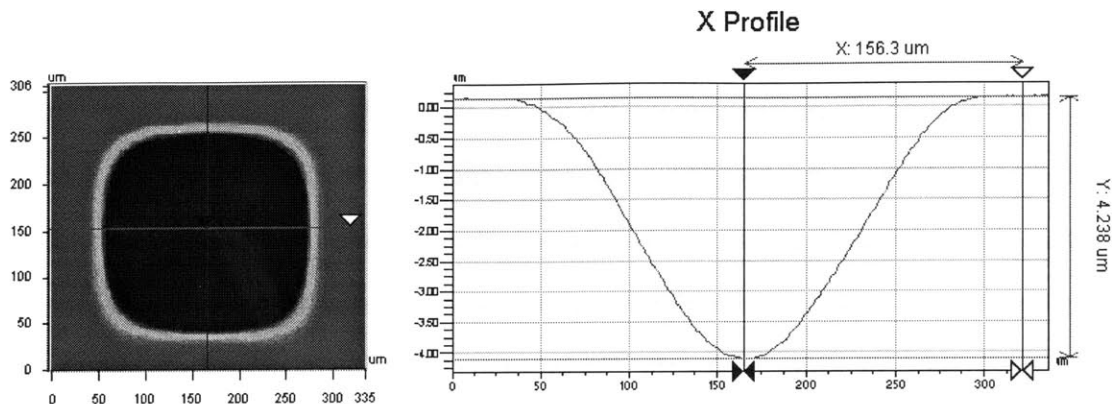
Figure 2-6. Quantitative measurements of the vertical profiles of the membranes are made using a Wyko optical profiler. The figure on the left shows a colored height contour generated by the Wyko analysis software. The plot on the right shows a cross-section through the center of a buckled membrane, from which the magnitude of the maximum deflection is measured.

change in light intensity was captured using a CCD camera. The images were demodulated and converted into a quantitative vertical profile of the sample surface, an example of which is shown in Figure 2-6. The maximum deflections of the buckled membranes were then measured. The sizes of the membranes were measured with a Vernier scale in an optical microscope using a 20X objective.

Calibration was carried out on a hot plate, on which a tape-mounted thermocouple sat side by side with the samples. Measurements were taken at various temperatures, from 24 to 110°C. At temperatures above roughly 75°C, the air flow near the sample became uneven and jerky, thus generating random noises in the measurement. A small fan was, therefore, placed at a distance from the setup, blowing air slowly towards the sample. As a result, although the air flow was still uneven, the noise generated became more regular and could be removed by averaging many measurements.

2.4.3   Thin Film Characterization

As a proof-of-concept demonstration, the stresses of evaporated chromium films were measured using the buckled membranes and curvature measurements. Prior to deposition, the baseline curvature of 290μm-thick (100) silicon wafers weres measured using the Tencor FLX-2320 thin film stress measurement system. The deflections of the membranes were measured with the Wyko optical profiler described in the previous section. The two samples were then cleaned twice in 3:1 sulphuric acid-hydrogen peroxide solutions for 10 minutes. After that, 500Å-thick chromium films were deposited at a rate of 2Å per second simultaneously using electron beam deposition on the samples. The pressure was maintained at about 5×10^{-7} torr throughout the deposition. The samples were then taken out of the deposition chamber for stress measurement. Measurements were taken every five minutes for the silicon wafer and roughly every two hours for the buckled membranes.

(a)   (b)
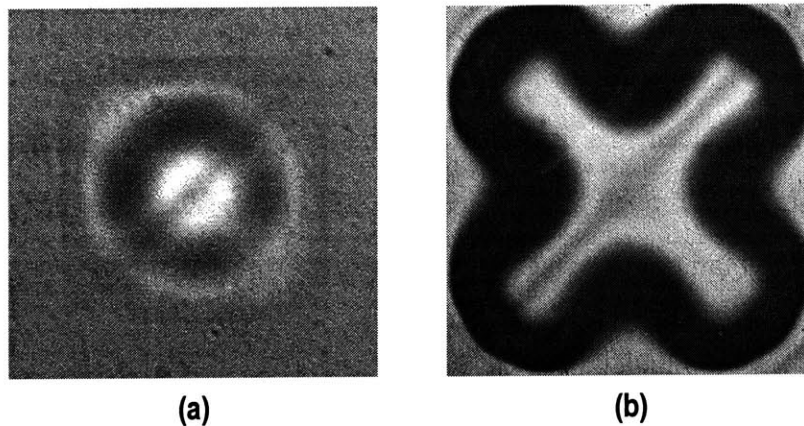
Figure 2-7. Optical images of buckled membranes in (a) the first buckling mode, and (b) a higher mode, at which point the structure no longer possesses rotational symmetry about the vertical axis.

2.5 Results and Discussion

Figure 2-7 shows the optical images, taken using Normaski optics, of two membranes of different sizes viewed from the top. The smaller membrane buckles in the first mode whereas the bigger one buckles in a higher mode, as evidenced by the break from rotational symmetry about the vertical axis. Figure 2-8 shows a comparison of the actual shape of a membrane in the first buckling mode and the approximate displacement function used in equation (2.6). It is apparent that the two shapes match, proving that the out-of-plane displacement function used in the analytic model is valid. The in-plane displacement functions, however, are unverifiable given the current technique and therefore remain as approximations. Figure 2-9 shows a plot of deflections versus membrane size. As expected, buckling occurs abruptly above a critical size. In the early stage of the post-buckling regime, the magnitude of the deflection increases rapidly with the size of the membranes. The rate of change slows considerably as the size becomes larger. It can also be seen, for a given membrane, that the buckled-down states have
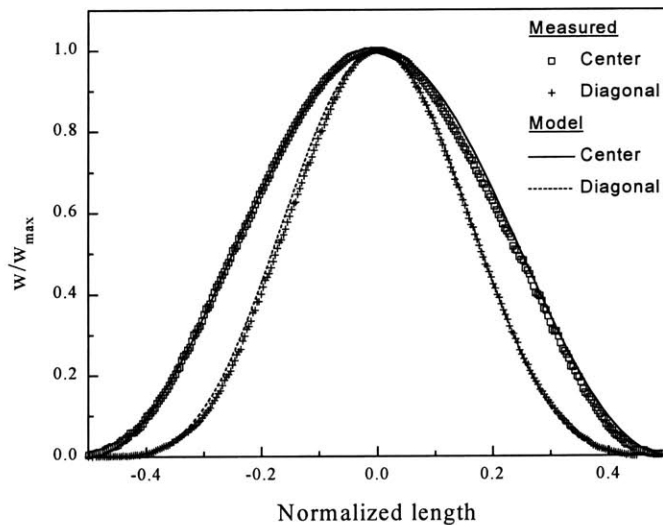
Figure 2-8. A comparison of the approximate displacement function and the actual shape of a membrane in the first buckling mode. The figure shows the vertical deflection profiles through the cross-section of the center and the diagonal of the membrane. Both shapes match.

41
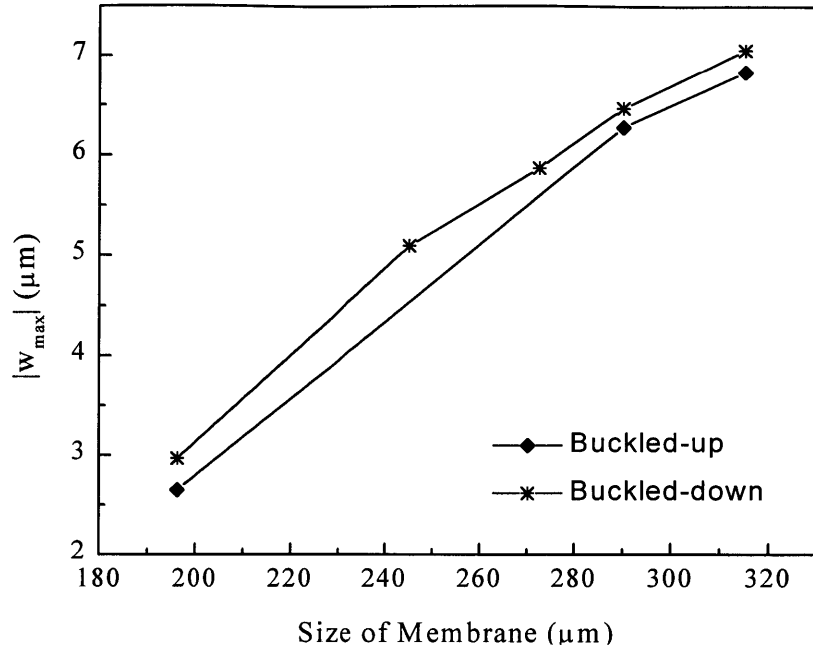
Figure 2-9. Deflection plotted as a function of the sizes of the membranes.

slightly larger deflections than the buckled-up states. This is a direct consequence of the bending-stretching coupling experienced by unsymmetric laminated plates, as clearly illustrated by the analytic model discussed in the previous section. Using the energy expression in equation (2.10), it can be shown that the buckled-down state, for a given membrane size, has a lower elastic strain energy than the buckled-up state. As a result, the buckled-down states are energetically more favorable than the buckled-up states. Nonetheless, if an initially flat membrane were to buckle, it should be equally likely to settle in either one of the two states because the flat position is located at a local energy maximum. However, nearly 90% of the as-fabricated membranes were found to be buckled-down. This is most likely because silicon dioxide, being hydrophilic and in contact with the etching solution, is slightly pulled towards the solution at the end of the etching process. As a result, when the membranes are released and become unstable, they tend to be trapped in the buckled-down states.
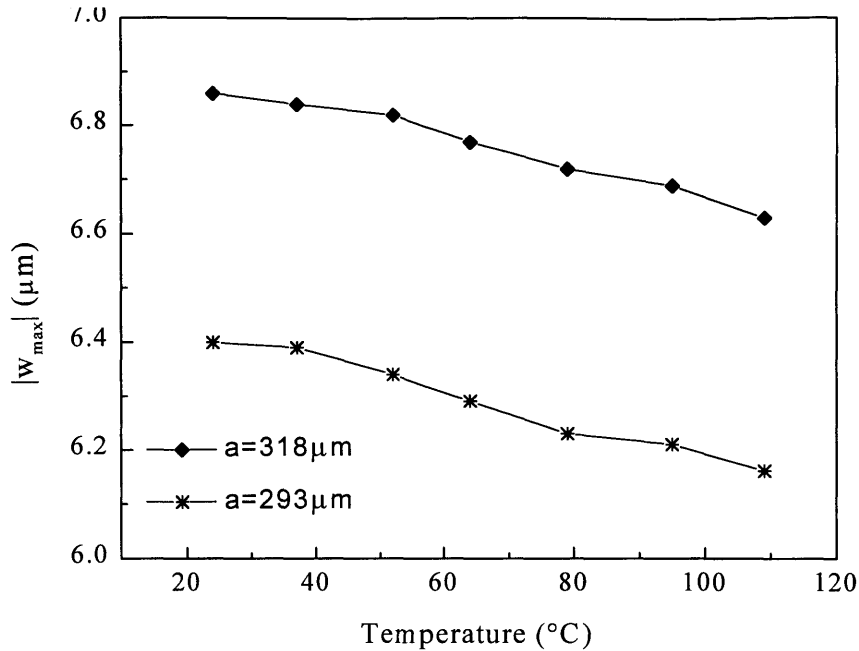
Figure 2-10. Deflection data for two membranes, plotted as a function of temperature.

Figure 2-10 shows deflections as a function of temperature for membranes of different sizes within one die. As temperature rises, the difference in thermal expansion of silicon and silicon dioxide results in a tensile stress. Consequently, deflections decrease with increasing temperature. Using equations (2.19) and (2.20), β_3 and S of this particular die are calculated from the calibration data as

$$\begin{cases} \beta_3 = 1.3 \times 10^{-6} \pm 0.15 \times 10^{-6} & MPa^{-1} - \mu m^{-1} \\ S = -498 \pm 63 & MPa - \mu m \end{cases}$$

The errors in β_3 and S are about 10-15%. This rather large variation is the result of measurement error incurred during calibration since the changes in deflections caused by heating are comparable in magnitude to measurement noises. In contrast, the variation in the product $\beta_3 S$, obtained from deflection data measured as a function of membrane size, is less than 1%. It has also been found that β_3 and S are not uniform across a wafer. The thickness variation in the silicon device layer, as a result of polishing, is believed to

contribute to the relatively large variation over a wafer in the extracted value of β_3, which has a linear dependence on thickness. Tightly spaced, multi-color contour lines, which indicate thickness variation, can be observed on the silicon device layer with the naked eye. In addition, the polishing step used to thin the silicon device layer may have also created localized stress in the bonded wafer.

Figure 2-11 shows a comparison between the stress measured using the curvature method, using thin wafers that are more sensitive to small stresses, and the SOI membranes after chromium deposition. Evaporated films were used for comparison instead of CVD films because, as explained in the previous chapter, CVD films do not cause curvature changes since the wafers are moment-balanced. It was observed that the stress of the chromium film was tensile and increased rapidly for the first few hours after
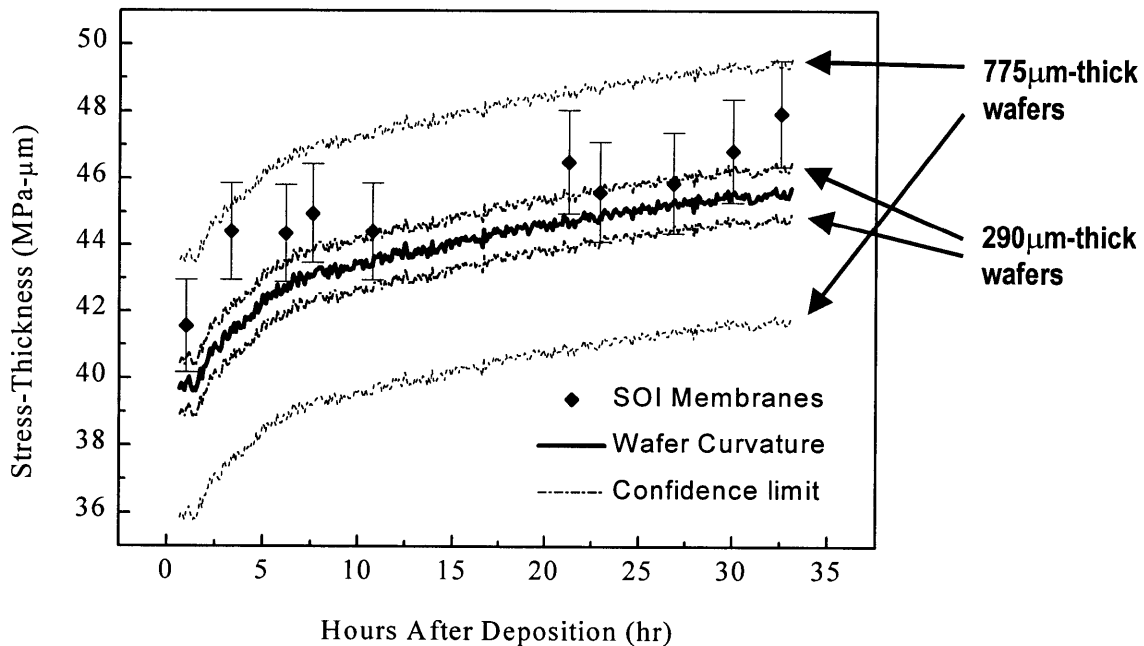
Figure 2-11. The stress of an evaporated chromium film measured using the curvature method (using especially thin wafers – 290μm-thick – that are more sensitive to small stresses) and the SOI membranes. The values only differ by about 5% and the trend in the stress evolution is matched. The confidence limit is also shown for the case if the wafers were 775μm thick.

44

deposition. The rate of change slowed to a stable value about 7 to 8 hours after deposition. The high tensile stress observed is consistent with the fact that evaporated chromium film, having the body centered cubic (BCC) structure, has a high melting point. This class of film materials, termed type I materials, is known to have a low mobility at room temperature. They exhibit only tensile stress with increasing film thickness. [Abe 90] The lack of stress relaxation during deposition, due to low atomic mobility at room temperature, results in high stresses at room temperature. The increase in stress after deposition is likely a result of grain growth, the exact causes of which are outside the scope of this work. By comparing the stress values obtained by the two techniques, it can be seen that the values differ by only about 5% and the error bars are comparable in magnitude. The trend in stress evolution was also captured correctly using the membrane technique. It should be noted that the wafers used for curvature measurements in this work are especially thin so that they are more responsive to small stresses. If thicker wafers with greater diameter were used instead, the confidence range would be much greater, as shown in the same figure.

In summary, we have demonstrated that the accuracy and sensitivity of the membrane technique are comparable to those of the curvature method. Improvements, which are laid out in greater detail in the next section, can be made to enhance the accuracy and sensitivity. The design allowed for the deposition of films on both sides of the membranes, making it suitable for measuring the stress in CVD films. The small sizes of the membranes also allowed for the construction of stress maps that quantitatively describe the stress distribution on wafers. Thus, it is apparent that the SOI membrane technique has proven to be a sensitive and useful stress measurement tool for CVD films.

2.6 Design of Next Generation Device

The next generation device should aim for three goals – enhanced sensitivity, better accuracy, and versatility.

To enhance device sensitivity, the membranes should, in general, be made less rigid so that deflections are greater and more easily measurable for a given stress. This can be achieved through several means. First, the thickness of the membranes should be reduced. One added advantage of having a thinner silicon dioxide layer is the reduction of the thickness-averaged stress in the membranes, which will result in an increase in the critical buckling size. As a result, membranes that buckled in the first mode are in general larger and therefore easier to be toggled between the buckled-up and buckled-down states. Second, the edges of the membranes can be aligned to the <100> directions, instead of the <110> directions, of the silicon device layer to take advantage of the smaller plate modulus. The plate modulus ($E/1 - \upsilon^2$) is the relevant elastic quantity that describes the rigidity of plates. It should be noted that while the in-plane biaxial modulus ($E/1 - \upsilon$) of (100) silicon wafers is isotropic, its in-plane plate modulus is, however, anisotropic. Third, the substrate material can also be changed to ones that are more compliant.

As demonstrated previously, the coefficients in the analytic expression are found either by applying a known stress to the actual devices or by comparing the expression with finite element modeling. While the former method has proven to be adequate, the small difference in thermal expansion between silicon and silicon dioxide has led to a calibration error of roughly 10% and has therefore limited the accuracy of the technique. Comparison with finite element modeling, though time-consuming, may eventually lead

to better accuracy. In addition, the remaining two coefficients, β_1 and β_2, can both be obtained from finite element modeling, resulting in three equations relating material properties to experimental measurements. Hence, elastic properties of the film may potentially be extracted in addition to the stress of the film. However, accurate device metrology, especially accurate knowledge of the thickness of the films, will then become important since the coefficients have up to a cubic dependence on thickness. Etch steps, such as holes in the silicon layer, should be patterned on the front side of the wafer so that the thickness of the silicon can be measured with a surface profilometer. The thickness of the exposed silicon dioxide layer in the etch steps can then be measured with an ellipsometer.

Although this work focuses exclusively on SOI membranes, it should be noted that the proposed methodology applies to any general composite membrane. For example, single crystal silicon can be replaced by polysilicon if substrate orientation is not a concern. In addition, additional layers, such as diffusion barriers and seed layers for electrodeposition, can be deposited on the membranes prior to the deposition of the film of interest. This is possible because only the *changes* in buckling and post-buckling responses are utilized to extract the stress of the film. The versatility in the choice of substrate material is an advantage few existing MEMS techniques are able to attain.

2.7   Summary

In this chapter, we described the design, fabrication, modeling, calibration, and testing of SOI membranes for the ex-situ stress measurement of thin films, in particular CVD films. The design allowed for the fact that CVD films deposit on both sides of a

47

wafer, which was a major hurdle for the use of the curvature method. The use of MEMS devices also allowed for the construction of stress maps that describe the stress distribution on wafers. The use of composite membranes also eliminated the need for the film of interest to be patterned or to be in contact with aggressive chemical etchants, which would otherwise damage the film. Experiments with an evaporated chromium film showed that both the accuracy and sensitivity of the measurements made using SOI membranes are comparable to those of the widely used curvature method for $290\mu m$ thick silicon wafers. In addition, several methods were proposed to improve the sensitivity, accuracy, and versatility of this technique.

Chapter 3

In-Situ Technique: *Stress Pointers*

3.1 Introduction

In the previous chapter, we presented the use of buckled SOI membranes to extract the stress and, potentially, the elastic properties of as-deposited thin films. The buckling technique is, however, not an ideal tool for in-situ use. A number of challenges remain to be addressed in order to design devices with true real-time and on-chip measurement capabilities. First, optical sensing techniques, such as those based on the use of laser beams and optical detectors, require clear optical paths to the wafers, which are difficult to realize in batch processing equipment like CVD tube reactors where wafers are placed side by side. Hence, the use of optical-based techniques, such as the SOI membranes and the curvature method, is essentially excluded. Second, for most real-time techniques, special fixtures, such as wafer holders and electrical wiring, are usually required to be installed in the deposition equipment. The disruptions caused by the installation not only hamper existing manufacturing process, but may also irreversibly damage the equipment. For example, electrical wiring may act as antenna inside a

plasma-enhanced CVD system and interfere with the plasma discharge, thus adversely affecting process uniformity and repeatability. Consequently, real-time measurement techniques will likely have only limited applications in commercial deposition systems.

In this chapter, we will describe the design and fabrication of a set of MEMS structures, called stress pointers, that are based on mechanically amplified rotation and the novel concept of "footprinting". These devices, instead of measuring stress in real time, mechanically record the evolution of stress as a function of film thickness during the formation of CVD films. The data is then extracted in ex-situ measurements after the deposition.

The concept of mechanically amplified rotation was first proposed and applied to MEMS by Wilner [Wil 92], whose design is shown schematically in Figure 3-1. The suspended structure shown was composed of two opposing beams that were fixed at one end to a frame and hinged at the other end to a gauge needle, located in between the two fixed-hinged beams. The two hinged junctions were slightly offset from each other. When the structure was released through the removal of the underlying sacrificial layer,
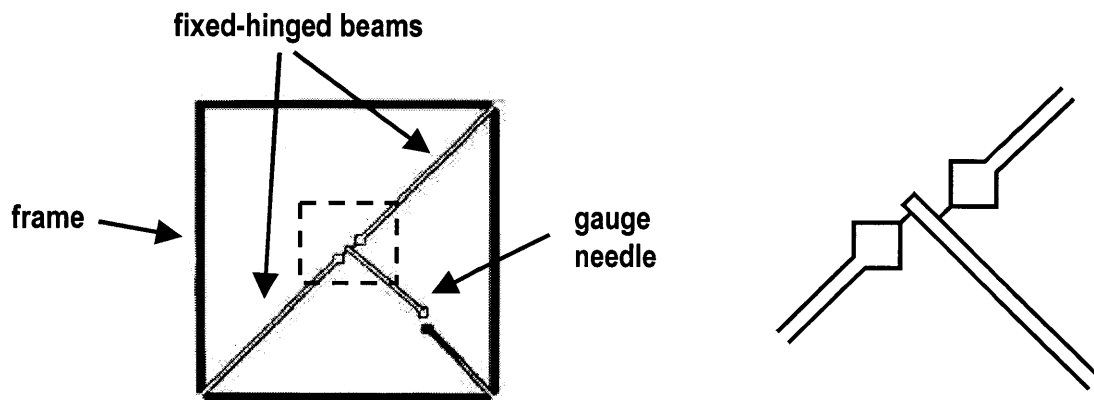
Figure 3-1. Schematic of Wilner's strainmeter. A magnified view of the junctions connecting the fixed-hinged beams and the gauge needle is shown on the right. [Wil 92]

50

the residual stress in the beams was relaxed, slightly changing the dimensions of the beams. The offset between the two beams caused the gauge needle to turn. The magnitude of the lateral deflection at the end of the gauge needle was large enough to be measured optically. However, the mechanical response of the structure was complicated because the hinges connecting the gauge needle and the fixed-hinged beams were not perfect and acted like springs. As a result, finite element simulations had to be performed to extract the stresses in the beams. The need to perform finite element calculation for every measurement had made this technique very unattractive for practical applications. Since then, more sophisticated designs with simpler mechanical responses and higher magnification have been developed [Dri 93, Eri 95, Lin 97, Pan 99], from which sensitive ex-situ strain measurements have been performed on the materials that constitute the structures.

In this work, we have adopted the indicator structure designed by Lin et al. [Lin 97], shown in Figure 3-2, as the starting point of our design. The indicator structure is constructed using a two-mask process, in which suspended polysilicon beams are formed by removing a layer of sacrificial oxide underneath the polysilicon film. The entire structure is attached to the silicon substrate at the two anchors only. With no constraint, the stress in the polysilicon is relaxed, slightly changing the dimensions of the beams. The test beam on the left of the structure magnifies this small change in dimension by rotating the slope beam in the middle, resulting in a small rotation of the indicator beam. The indicator beam turns right if the polysilicon is in compression, and left if it is in tension. The lateral displacement at the tip of the indicator beam, which is equipped with a Vernier gauge, is then measured optically with a microscope. The mechanical responses of the beams was modeled by Lin et al. using simple force and moment balances. Ignoring the spring effect of the slope beam, the stress in the polysilicon, σ, is related to the lateral deflection, δ_v, of the tip of the indicator beam as

51

$$\sigma = \frac{2}{3C} \frac{E}{1-\upsilon} \frac{L_{sb}}{L_{ib}L_{tb}} \delta_v, \tag{3.1}$$

where $E/1-\upsilon$ is the biaxial modulus of polysilicon, L_{sb}, L_{ib}, and L_{tb} are the lengths of the slope beam, indicator beam, and test beam respectively. C is a correction factor due to the presence of the indicator beam, which is given by
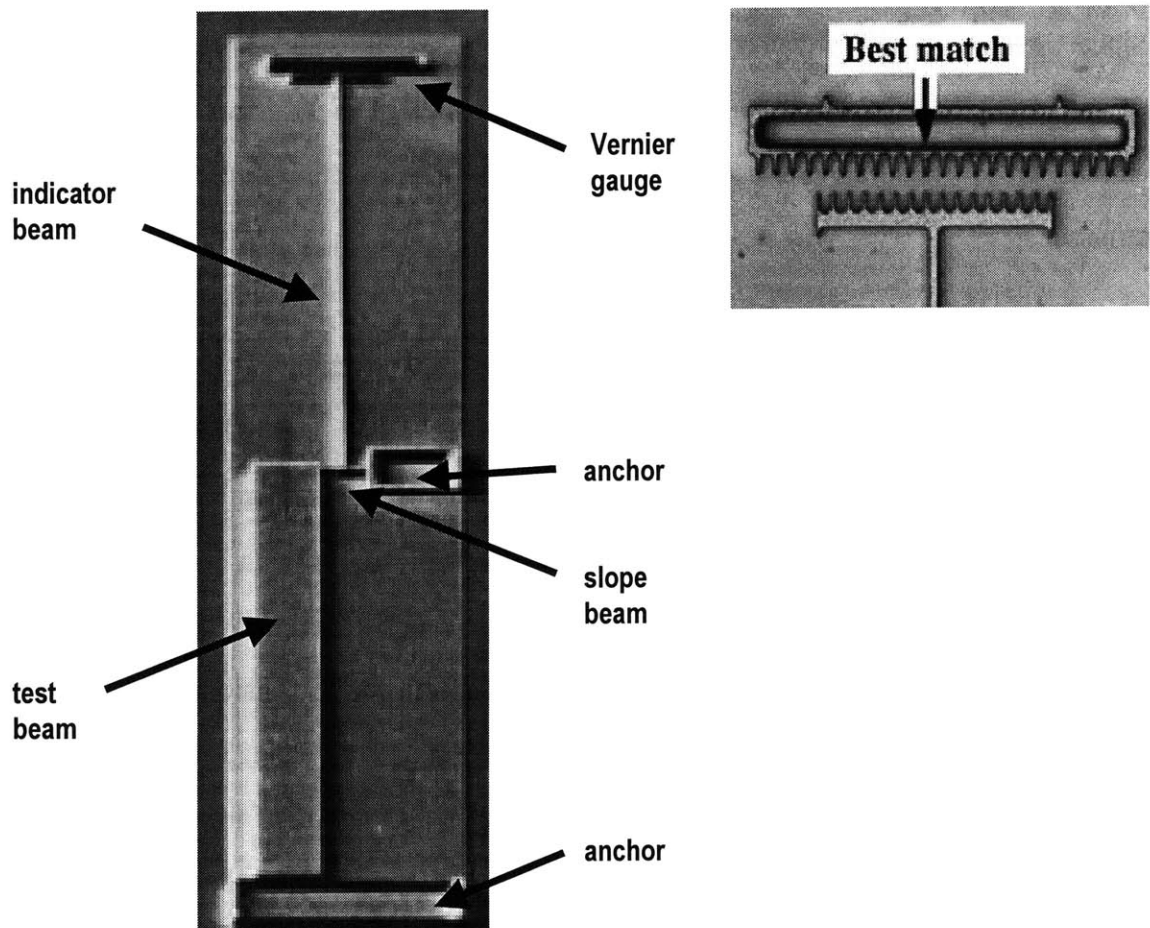
Figure 3-2. SEM photographs of Lin's indicator structure. After sacrificial oxide release, the test beam slightly changes in dimensions due to stress relaxation. This small change is converted into a rotation of the slope beam, which, in turn, causes the indicator beam to rotate. The indicator beam turns right if the polysilicon is in compression, and left if it is in tension. The displacement at the tip of the indicator beam is then measured optically by referencing the Vernier scale. A close-up image of the Vernier gauge, showing a tensile stress reading, is shown on the right. [Lin 97]

$$C = \frac{1 - d^2}{1 - d^3}$$

(3.2)

where d is the ratio of the width to the length of the indicator beam.

3.2   Sensor Design and Device Layout

Building upon the design of Lin's indicator structure, we have added two new features to the design of stress pointers. Figure 3-3 shows an optical photograph of the top half of a stress pointer built in this work, whose dimensions are listed in Table 3-1. The particular features of this design will be discussed in detail later in this section.
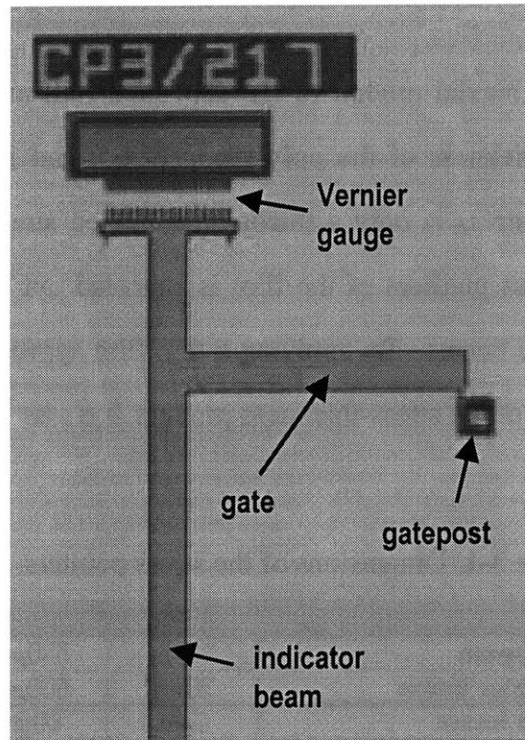
Figure 3-3. Optical photograph showing the top view of a stress pointer. Two new structural elements were added to the design – gate and gatepost. The gate in this particular stress pointer is 217μm long and the separation between the gate and the gatepost is 3μm. This particular device was designed specifically for measuring compressive stress.

First, the structures are no longer used solely for measuring the stress in the polysilicon film. Instead, the stress of a thin film is measured by depositing the film on the released structures. The stress of the film will slightly change the dimensions of the test beam, which, in turn, causes a further rotation of the indicator beam. The change in lateral displacement, $\Delta\delta_v$, is then measured with the Vernier gauge. An important requirement is that films must be deposited uniformly on both the top and bottom of the beams or the indicator beam will bend, resulting in erroneous readings. Films formed by CVD potentially satisfy this requirement. Ignoring contributions from films deposited on the sidewalls of the beams, it can be shown (see Appendix B), by using a force balance, that the change in lateral displacement is related to the stress of the deposited film, σ_f, as

$$\sigma_f = \frac{2}{3C}\left(E_f + \frac{h_s}{2h_f}E_s\right)\frac{L_{sb}}{L_{ib}L_{tb}}\Delta\delta_v, \tag{3.3}$$

where E_f and E_s are the biaxial moduli of the deposited film and the polysilicon beam respectively, h_s is the thickness of the polysilicon beam, and h_f is the film thickness. Note that the measured stress is only a thickness-averaged stress because any bending effect caused by the stress gradient of the film is canceled out by having two identical films on both sides of the beams. By applying a thin film approximation, equation (3.3) can be rewritten in terms of the stress-thickness product $h_f\sigma_f$ as

Table 3-1. Dimensions of the stress pointers.

Structure	Width	Length
Test beam	$30\mu m$	$500\mu m$
Indicator beam	$30\mu m$	$500\mu m$
Slope beam	$5\mu m$	$60\mu m$
Vernier fingers	$2\mu m$	$10\mu m$
Gate	see Table 3-2	
Gate Separation	see Table 3-2	
Center to center separation of Vernier fingers		
(at the indicator beam)	$5\mu m$	
(at the anchor)	$4\mu m$	

$$h_f \sigma_f = \frac{E_s h_s}{3C} \frac{L_{sb}}{L_{ib} L_{tb}} \Delta \delta_v. \qquad (3.4)$$

The second difference between the two designs is that two closely-spaced structural elements, labeled as "gate" and "gatepost" in Figure 3-3, are included in the structure for in-situ stress measurement. As illustrated schematically in Figure 3-4, during the formation of CVD films, the indicator beam gradually turns due to the stress of the film. The gate, being attached perpendicularly to the indicator beam, also turns and slowly approaches the gatepost. Meanwhile, the film of interest is deposited on all the surfaces of the beams, and in particular, on the sidewalls of the gate and the gatepost. As a result, the separation between the gate and the gatepost, d, is slowly reduced. The gate eventually touches the gatepost and is welded to it by the depositing film. Once locked in place, any change in stress or film thickness will not bring about further rotation to the indicator beam. Thus, the stress and thickness of the film at this particular instant are permanently recorded by the structure in the form of a mechanical rotation. The point at which lock-in occurs is set by the length of the gate L_g and the initial separation distance
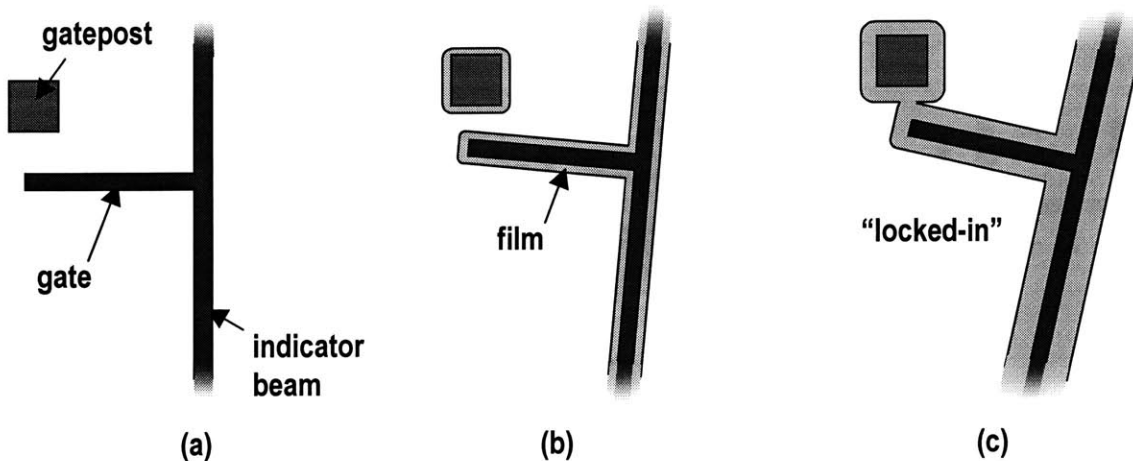
Figure 3-4. Schematic of the lock-in mechanism – **(a)** The gate and the gatepost are separate and parallel to each other in as-fabricated structures if the polysilicon film has zero stress; **(b)** during film formation, the indicator beam turns and the film fills the gap between the gate and the gatepost, reducing the separation between the two; **(c)** eventually, the gate touches the gatepost and is locked-in, with the separation being two times the film thickness at the time of the lock-in. (Drawings not to scale.)

d_o. The longer the gate is, the lower the stress and film thickness are when the gate is locked-in. Also, the greater the initial separation is, the higher the stress and film thickness product is when lock-in occurs. Hence, the stress and thickness of the film at any given moment, from low to high stress and film thickness, can be extracted by choosing the appropriate device dimensions – L_g and d_o. To calculate the relationship between the film thickness and the lateral displacement at lock-in, it is assumed that the structures have straight edges and sharp corners. Using simple geometric construction, as illustrated in Figure 3-5, it can be shown that the film thickness at lock-in is given by

$$h_f = \frac{1}{2}\left(d_o - \frac{L_g}{L_{ib}}\delta_v^{total}\right), \tag{3.5}$$

where δ_v^{total} is the *total* lateral displacement, including the initial displacement due to the stress in the polysilicon beam.

Combining equations (3.3) and (3.5), we obtain two simultaneous equations,

(a) **(b)** **(c)**
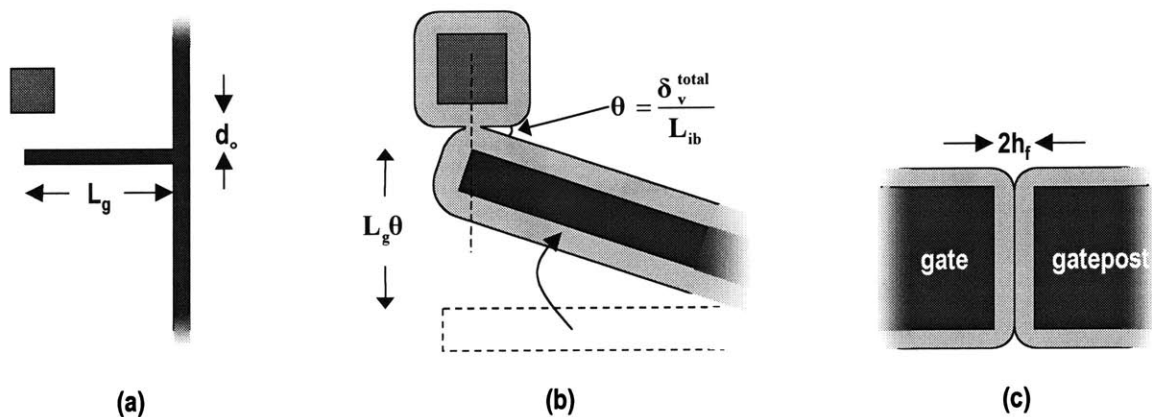
Figure 3-5. Determination of the relationship between the film thickness at lock-in and the total lateral displacement – **(a)** the gate length and separation distance are given by L_g and d_o, respectively, before film deposition; **(b)** the geometry when lock-in occurs; **(c)** schematic diagram showing that the separation distance is two times the film thickness at lock-in (the location of this cross-section is indicated by the straight dotted line in (b). (Drawings not to scale.)

56

$$\begin{cases} \sigma_f = \dfrac{2}{3C}\left[E_f + \dfrac{E_s h_s}{\left(d_o - \dfrac{L_g}{L_{ib}}\delta_v^{total} \right)} \right]\dfrac{L_{sb}}{L_{ib}L_{tb}}\Delta\delta_v \\[4mm] h_f = \dfrac{1}{2}\left(d_o - \dfrac{L_g}{L_{ib}}\delta_v^{total} \right) \end{cases} \qquad (3.6)$$

from which both stress and film thickness can be calculated, given L_g and d_o, by measuring the lateral displacement before and after film deposition.

A single stress pointer is capable of measuring only a unique set of stresses and film thicknesses, represented by the curve in Figure 3-6, which we shall call the device trajectory. The curve is constructed using equation (3.6), by plotting σ_f as a function of h_f. On the left of the trajectory is the regime in which the gate and the gatepost are not yet locked-in, thus the structure is free to turn. Whereas on the right is the regime in which lock-in has occurred and the structure is no longer free to move. The point at
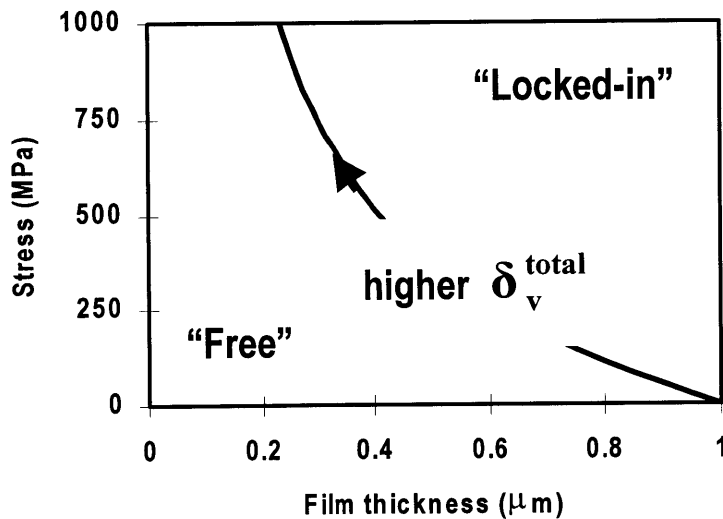
Figure 3-6. Any pointer structure with a given L_g and d_o, crosses over from the "free" to the "locked-in" regime at a unique combination of stress and film thickness, represented by the device trajectory in the figure. The exact point at which the cross-over occurs is measured by the total lateral displacement.

which the structure crosses over from the "free" to the "locked-in" regime, which is measured in terms of δ_v^{total}, indicates what the stress is at a certain film thickness. Extending this idea further, if there are a large number of structures with different geometry, specifically L_g and d_o, the evolution of stress as a function of film thickness can be recorded in-situ without real-time measurements. This leads to the concept of "footprinting", as illustrated schematically in Figure 3-7. Shown in this figure is a contour plot consisting of device trajectories similar to the one shown in Figure 3-6. Each trajectory represents a structure with different geometry. Two different sets of structures are designed for measuring tensile and compressive stresses separately. The structures are designed in such a way that their trajectories cover as much area in the stress versus film thickness plot as possible. During film formation, stress evolves with film thickness, thus continuously crossing over from the "free" to the "locked-in" regimes of the various structures. Structures with longer gate or shorter separation
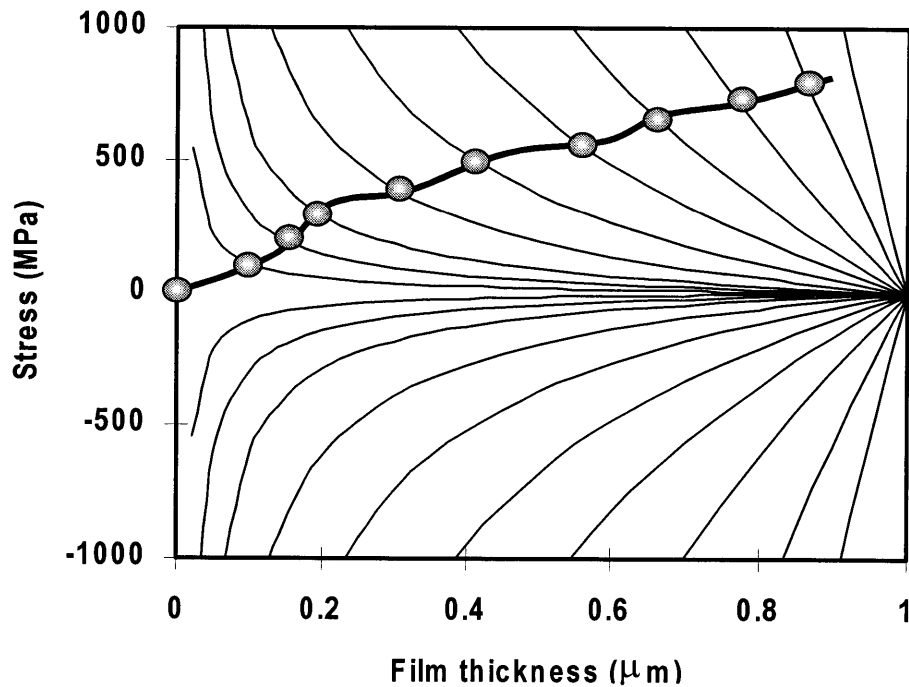
Figure 3-7. A much simplified contour plot showing an imaginary stress curve intersecting a series of device trajectories at the dots. "Footprints" of the stress evolution are captured as a function of film thickness by the lock-in of structures with various geometry, specifically L_g and d_o.

58

distance will become locked-in first, whereas those with shorter gates or greater separation distances will lock-in later or remain free. "Footprints" left behind by the stress evolution are traced by the mechanical rotations of the stress pointers. Table 3-2 lists the geometric configurations of the gates and the gateposts used in the current work.

Table 3-2. Geometric configurations of the gate and gatepost used in this work.

Lg (μm)								
d_o=1μm		d_o=2μm	d_o=3μm				d_o=5μm	
148	412	207	42	68	113	217	78	103
155	432	217	43	70	116	225	79	104
163	454	228	44	71	119	235	80	105
171	477	239	45	73	122	245	81	107
180	501	251	46	75	125	256	82	108
189		264	47	76	129	267	83	110
198		277	48	78	133	280	84	111
208		291	50	80	136	294	85	113
218		305	51	82	140	309	86	114
229		321	52	84	145	324	88	116
241		337	53	86	149	340	89	118
253		353	54	88	154	357	90	119
265		371	56	90	159	375	91	121
279		390	57	92	164	394	92	123
293		409	58	95	169	414	93	124
307		430	59	97	175	434	95	126
323		451	61	99	181	456	96	128
339		474	62	102	187	479	97	130
356		497	64	104	194	503	98	
374			65	107	201		100	
392			67	110	209		101	

3.3   Device Calibration

As mentioned earlier in the chapter, the mechanical responses of rotational structures are typically determined by finite element modeling because the hinges are difficult to analyze. One way to get around this problem is to build calibration structures,

shown in Figure 3-8, alongside the device structures. The calibration beam is affixed to the test beam at one end and to the substrate at the other. When the structure is released, the test beam and the calibration beam both undergo dimensional changes that are opposite in direction. As a result of this strain, the two beams exert a force on each other, the magnitude of which depends on the width and the length of the two beams. The displacement at the slope beam, therefore, is dependent on the stress in the beams as well as the widths and lengths of the two beams. Mehregany et al. [Meh 87] have shown that the displacement at the junction of two beams with dissimilar widths and lengths, $\Delta \ell$, is given by

$$\Delta \ell = \frac{\sigma}{E} \frac{1}{w_{tb} - w_{cb}} \left(\frac{w_{tb}}{L_{tb}} + \frac{w_{cb}}{L_{cb}} \right),$$ (3.7)

where w_{cb} and L_{cb} are the width and the length of the calibration beam, respectively.
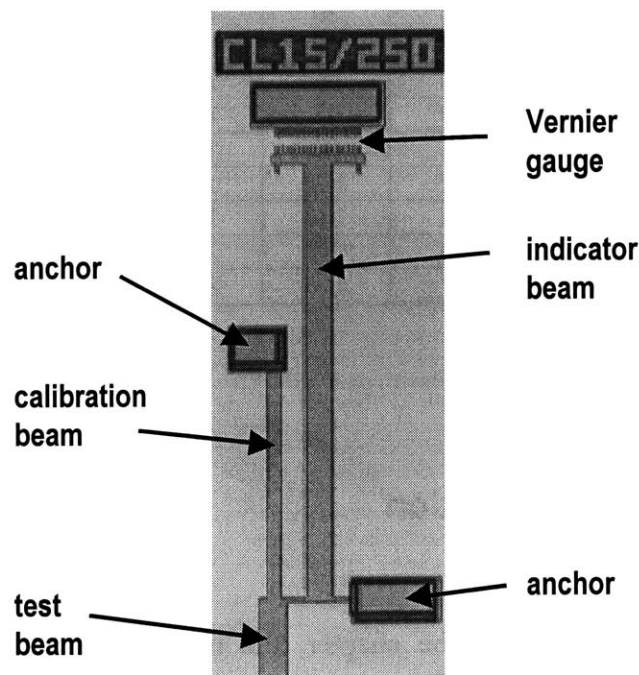

Figure 3-8. Optical photograph of a calibration structure. The calibration beam in this particular structure is 15μm wide and 250μm long. It modifies the displacement at the junction with the test beam and thereby changes the displacement of the Vernier gauge. Calibration is carried out by having structures like this one with various widths.

60

Therefore, the length change of the test beam and the displacement of the indicator beam are modulated by the width and length of the calibration beam. By having an array of these structures with different widths and lengths, an empirical relationship correlating the change in length of the test beam and the displacement, δ_v, is obtained. The calibration beams used in this study are 250μm long, with widths ranging from 15 to 55μm.

3.4 Experiment

3.4.1 Fabrication

Figure 3-9 shows the process flow for the fabrication of the pointer structures. First, a roughly 2μm-thick low-temperature oxide (LTO) was deposited on 525μm-thick (100) silicon wafers using low pressure chemical vapor deposition (LPCVD). This oxide layer served as the sacrificial oxide. It was densified at 950°C for one hour in a nitrogen atmosphere and was then patterned using reactive ion etching with a 3:1 CF_4-CHF_3 gas mixture, to form captured oxide supports shown in Figure 3-9(i). The baseline radii of curvature of the wafers were measured at this point. Next, a LPCVD polycrystalline silicon with a nominal thickness of 2μm was deposited to form the structural layer. The polysilicon was covered with a 500Å-thick LTO capping layer and implanted with 7×10^{15} cm^{-2} of Phosphorous at an energy of 170keV. The implanted wafers were annealed at temperatures from 900 to 1000°C, resulting in residual stresses ranging from -30MPa to -5MPa in compression. The LTO capping layer was then stripped using a buffered oxide etch (BOE). Polysilicon on the backside of the wafers was etched away using reactive ion etching with a 1:1 Cl_2-HBr gas mixture. After backside etching, the radii of curvature

61
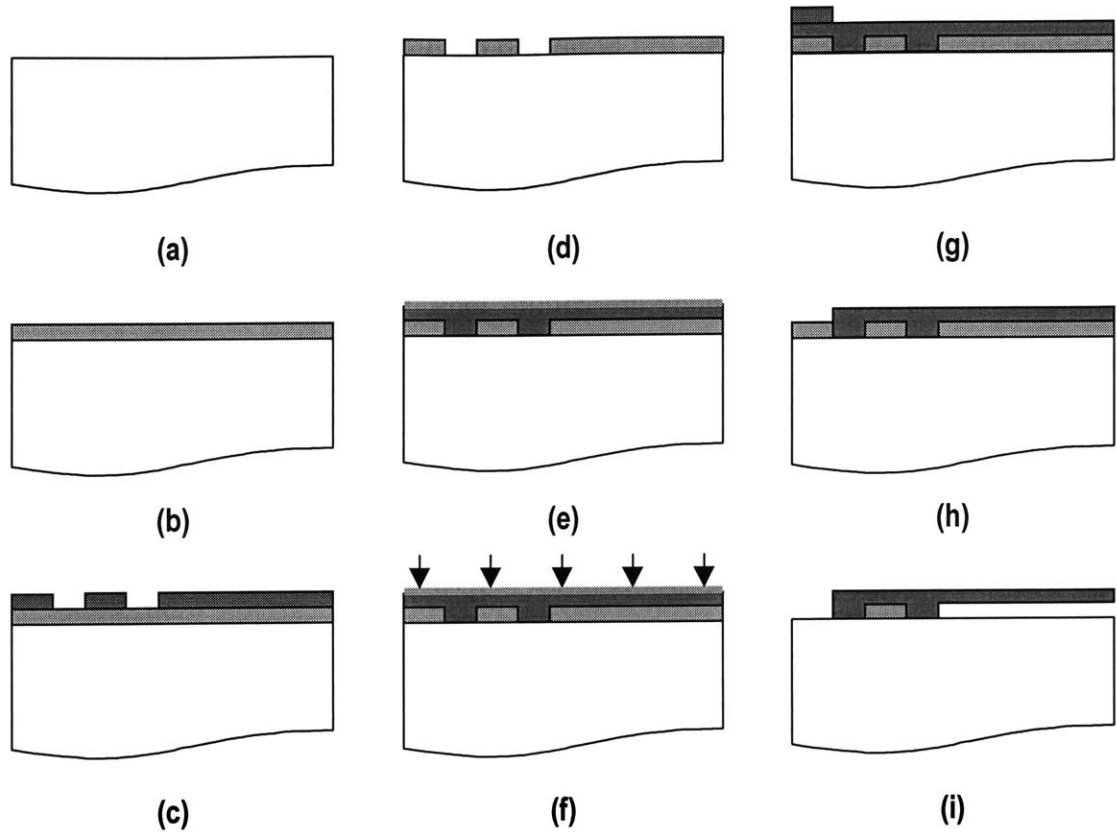
Figure 3-9. Fabrication of the stress pointers (pictures shown are the cross-sections through one of the anchors) – **(a)** (100) silicon wafer; **(b)** 2μm-thick LTO silicon dioxide; **(c)** supports are patterned with photoresist; **(d)** silicon dioxide is etched using reactive ion etching; **(e)** 2μm-thick LPCVD polysilicon and 500Å-thick LTO silicon dioxide implant cap; **(f)** Phosphorous implant at a dose of $7 \times 10^{15} \text{cm}^{-2}$; **(g)** beams are patterned with photoresist; **(h)** polysilicon is etched using reactive ion etching; **(i)** the silicon dioxide sacrificial layer is stripped by 49% hydrofluoric acid.

of the wafers were measured again to obtain the average stress in the polysilicon layer. The structures were then patterned to form the pointers. Next, the full wafers were diced into 1.5cm × 1.5cm dies. The dies were then cleaned twice in 3:1 sulphuric acid-hydrogen peroxide solutions. The sacrificial oxide was removed through a ten minute etch in concentrated 49% hydrofluoric acid solution (HF). After rinsing, the dies, with DI water on top, were immersed in 2-propanol for solvent exchange. The alcohol on the surface of the dies was subsequently boiled off on a hot plate to prevent the beam structures from sticking to the surface of the substrate.

3.4.2 Thin Film Characterization

After release and drying, a 0.4μm-thick silicon nitride film was deposited by plasma-enhanced CVD (PECVD) on the devices for a proof of concept. Prior to deposition, the temperature of the wafer stage was set to 80°C and was allowed to equilibrate for at least one hour. The samples were then placed on dummy wafers, which were transported into the deposition chamber automatically through a load lock. The base pressure inside the deposition chamber was maintained at around 10^{-4} torr. To deposit silicon nitride, $10 cm^{-3}s^{-1}$ of nitrogen gas and $113 cm^{-3}s^{-1}$ of SiH_4 gas were flowed into the deposition chamber. The power of the magnetron tube was set at 210W. The reflected power was constantly kept at zero. The resulting deposition rate was slightly above 6Å per second.

3.5   Results and Discussion

It has been found that the beams stick to the substrate, and thereby become non-functional, if the beam structures are allowed to dry without the alcohol boil-off process described above. In some cases, the beams remain stuck to the substrate even though they are released by alcohol boil-off. This was not a major problem in its original application by Lin et al. since strain measurements could be made with the structures submerged in DI water. In our case, however, the structures have to be dried. As a result, low-pressure CVD (LPCVD) films cannot be deposited on these structures since the wafers need to be cleaned by wet chemical etches, without the alcohol boil-off, immediately before LPCVD deposition.

Figure 3-10 shows SEM images of the fabricated structures. After the structures are released, the beam structures were found to bend down, which leads to unreliable strain readings. Several reasons may have contributed to the bending. One, stress gradients in the polysilicon film may lead to beam bending. This may also explain why beam bending was not observed by Lin et al. since the presence of stress gradients strongly depends on processing conditions. Two, the different levels of doping in the polysilicon and the single crystal silicon substrate may have induced a potential difference across the gap between the beam and the substrate, resulting in an electrostatic force large enough to bend the beams [Sri 99].

Despite the presence of beam bending, PECVD silicon nitride films were deposited on the stress pointers to determine whether the films could be deposited uniformly on the top and bottom of the beams. After deposition, it were found that the amount of film deposited on the top and bottom of the beams was not the same, as evidenced by the increased bending of the beams. This indicates that the assumption we made earlier in the development of equation (3.3) is invalid. The mechanical responses of the deposited structure, as a result, become very difficult to model unless the non-uniformity of the films is well characterized.

(a)   (b)   (c)
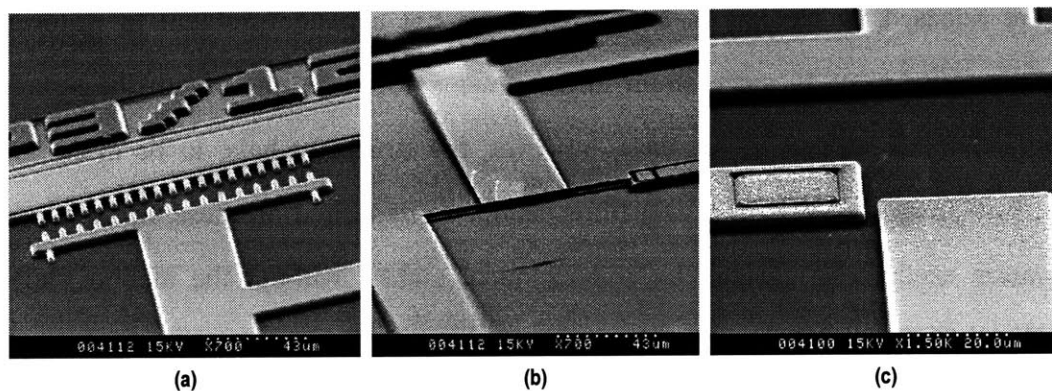
Figure 3-10. SEM images of the stress pointers – **(a)** indicator beam and Vernier gauge; **(b)** test beam and slope beam; **(c)** gate and gatepost.

It is concluded that there are two major shortcomings in the design of the stress pointers. One, the beams are too compliant in the vertical direction, making them vulnerable to stiction. Two, the beams are located too close to the substrate, thereby preventing the diffusion and deposition of gaseous reactants underneath the beams. The small separation between the beams and the substrate also facilitates stiction. Design changes that can potentially circumvent the above problems are laid out in greater detail in the next section.

3.6   Design of Next-Generation Device

A design for the next generation device is proposed in this section. The basic concept of the new design is essentially the same as the one used in the current work,
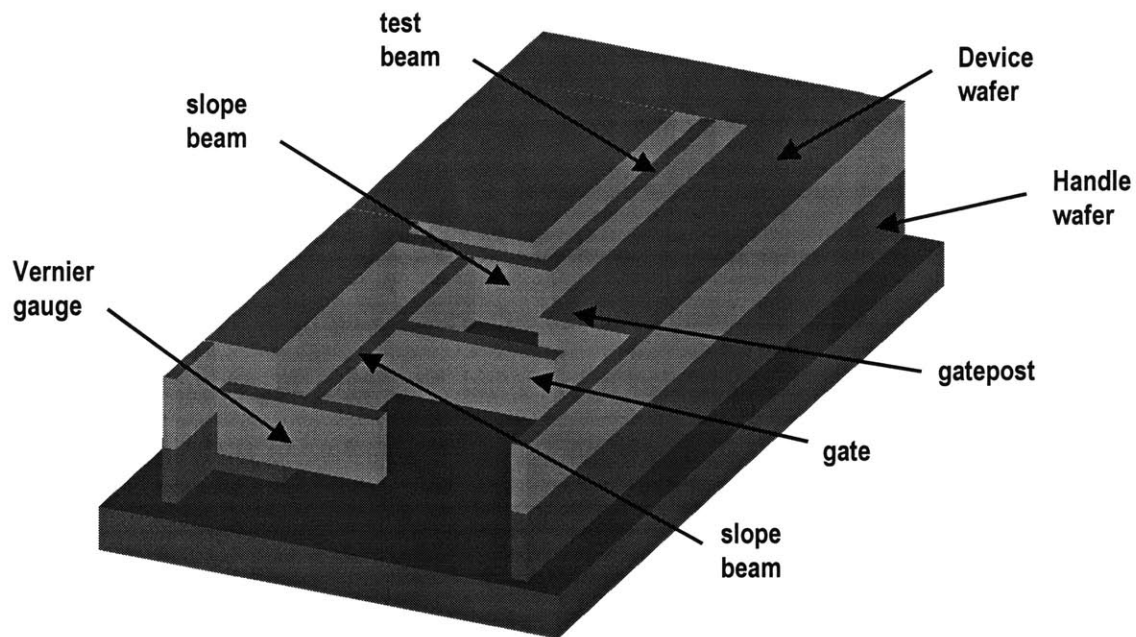
Figure 3-11. 3-D drawing showing the proposed design of the next generation device. The thickness of the structure is much greater than the width. As a result, the beams are much stiffer in the vertical direction.

65

except for the orientation of the beams, which are now rotated 90° about their longitudinal axes. In this configuration, the widths of the beams are much smaller than the heights of the beams, as illustrated in Figure 3-11. The heights of the beams should be on the order of 20 to 30μm. As a result, thickness variation resulting from wafer polishing will have little influence on the mechanical responses of the structures. Films that are deposited on the sidewalls of the beams now contribute to the displacement of the Vernier gauge whereas those deposited on the top and bottom of the beams only have small influence. LPCVD and PECVD films, therefore, can be deposited on the structures since they both have good sidewall coverage. The structures can be fabricated from bonded wafers using deep reactive ion etching, which is capable of etching deep trenches. The proposed fabrication process is shown in Figure 3-12.

This design potentially solves all the problems mentioned in the previous section. First, the beams are now separated significantly from their surroundings. As a result, they should no longer stick to the substrate even when alcohol boil-off is not performed. Second, the beams are thicker and thereby much stiffer in the vertical direction since the moment of inertia of a beam has a cubic dependence on the beam thickness. As a result, the beams should not bend under the influence of gravity. Third, the beams and the substrate now have the same level of doping. Consequently, there should not be any potential difference across the beams and the substrate. Single crystal silicon also has very little strain gradient, which also helps avoid bending. In addition, the elastic properties of the beams, which are important in the determination of stress, are now more accurately known.
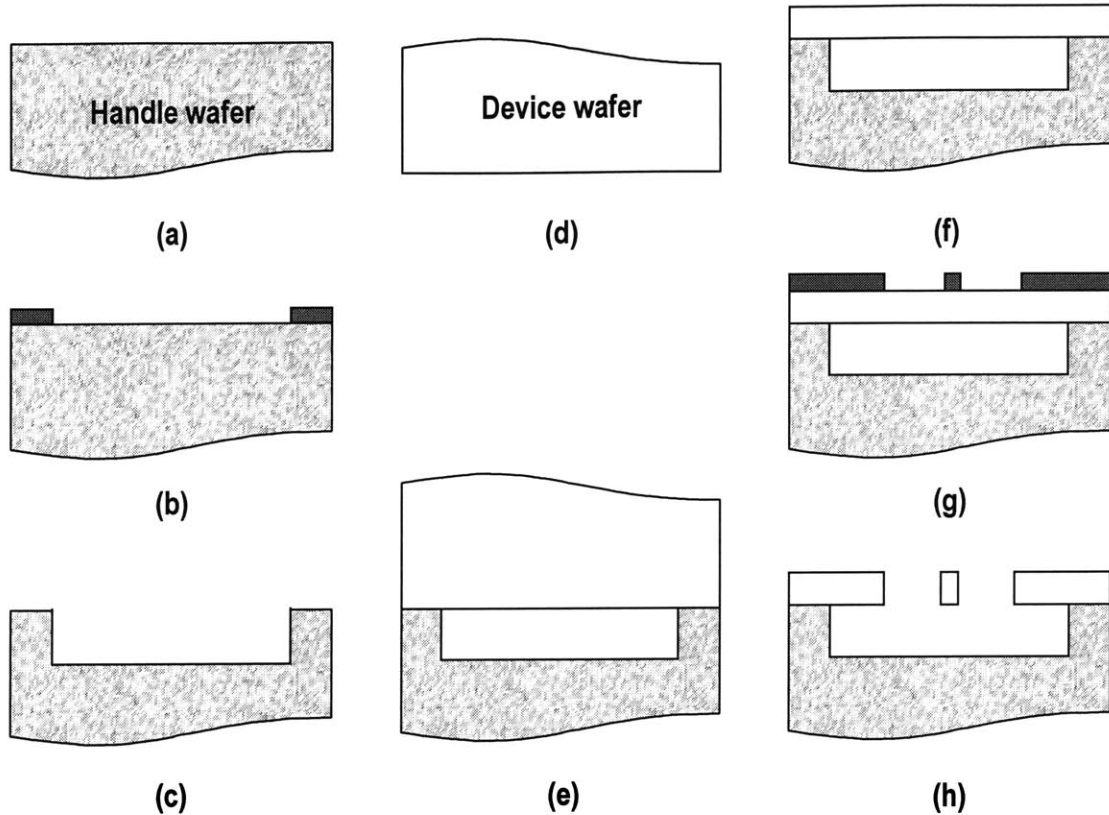
Figure 3-12. Fabrication process for the proposed new design for the stress pointers – **(a)** (100) silicon handle wafer; **(b)** a square opening is patterned with photoresist; **(c)** a basin is etched using deep reactive ion etching; **(d)** (100) silicon device wafer, with the same doping level as the handle wafer; **(e)** the two polished surfaces are fusion bonded; **(f)** backside of the device wafer is etched and polished to the desired thickness; **(g)** beam shapes are patterned with photoresist; **(h)** beams are etched by deep reactive ion etching.

3.7 Summary

We have designed and fabricated a set of MEMS structures, called stress pointers, for in-situ stress measurement of CVD films. The design is based on mechanically amplified rotation and the novel concept of "footprinting". Stress is recorded in-situ by the mechanical rotation of polysilicon beams, which stop turning at various pre-

determined film thicknesses, thereby measuring stress as a function of film thickness. The fabricated structures are found to bend significantly and stick to the substrate after drying. PECVD silicon nitride was deposited on the structures but the amount of film deposited on the top and bottom of the beams was not identical. An improved design that may potentially circumvent the above problems was proposed.

Chapter 4

Summary and Future Work

4.1   Summary of Results

Even though stress is not considered a defect per se, its presence can generate many types of defects that can lead to device failure. The ability to control the magnitude of stress during film deposition is, therefore, critical. However, the origin of stress in thin films remains a subject of intense debate, the understanding of which relies on our ability to make accurate and sensitive stress measurements during and after film formation. Based on the MEMS approach, this thesis accomplished this goal for one particular type of film – films deposited by CVD. This type of film is the most widely used in industry and yet, the formation of CVD films is the least well understood.

For ex-situ stress measurements, we have designed and fabricated buckled SOI membranes, the deflections of which depend on the average stress of the membranes. An analytic model has been developed and calibrated to model the mechanical responses of the buckled structures. By measuring the changes in the buckling behavior of the

membranes after film deposition, it has been demonstrated that the stress of the deposited film can be measured accurately. In particular, the stresses of an evaporated chromium film measured using the curvature method and the SOI membranes have been shown to agree to within 5%, and the error bars are found to be comparable in magnitude.

For in-situ stress measurements, we have designed and fabricated stress pointers, the rotations of which depend on both the stress and thickness of the deposited film. Stress is recorded as a function of film thickness in the form of a mechanical rotation, eliminating the need for real-time measurements. The fabricated structures were found to bend and stick to the substrate. In addition, PECVD films were found to be deposited at different thicknesses on the top and bottom of the beams. This precludes accurate modeling of the mechanical response. A new design that may potentially solve these problems has been proposed.

4.2   Future Work

From conception to mass production, it is typical for a product to go through several stages of development before every parameter is optimized. This thesis has proposed and demonstrated the use of two novel MEMS structures for ex-situ and in-situ stress measurements of CVD films. Results obtained from first generation devices suggest that several improvements can be made to the structures to achieve better accuracy, enhanced sensitivity, and greater versatility. Guidelines for the design of next generation devices have been laid out in great detail at the end of Chapters 2 and 3.

The goal, as mentioned earlier, for the design of stress measurement tools is to understand the origin of stress in thin films. Alongside the development of more advanced stress measurement devices, materials research should be carried out, using the new capabilities given by the new devices, to further the understanding of stress generation mechanisms. The results obtained can be used, in turn, to design better stress measurement devices with well-controlled stress and elastic properties. Ultimately, the stress and elastic properties of thin films should be controlled with ease by altering processing conditions such as temperature, flow rate, and base pressure, during film deposition.

Appendix A

Location of the Neutral Plane

In thin plate, there exist two planes with practical significance – the middle plane and the neutral plane. Suppose we have a plate in the Cartesian coordinate system oriented in such a way that the two faces of the plate are parallel to the x-y plane and the thickness is measured along the z-axis. In this case, the middle plane is usually defined as the plane that is parallel to the x-y plane and is equidistant from the top and bottom of the plate. In other words, the middle plane is *the* middle plane of the plate. The neutral plane, on the other hand, is defined as the plane that is parallel to the x-y plane and remains unstretched when a curvature is applied to the plate. This is illustrated in Figure A-1. When a homogeneous, isotropic plate is bent, one half of the plate is in tension and the other half is in compression. The plane that is unstretched naturally coincides with
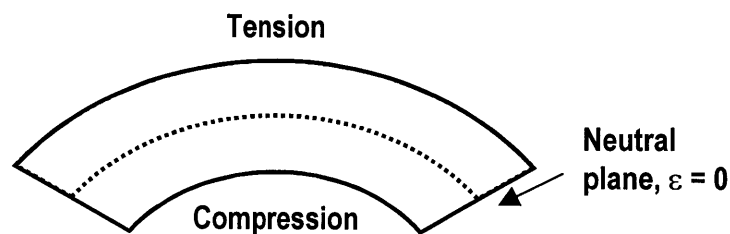

Figure A-1. Cross-section of a bent isotropic plate, illustrating the stress state and the location of the neutral plane.

the middle plane due to symmetry. Therefore, in most cases, these two terms are used interchangeably. This is, however, not the case for composite plates.

Suppose a curvature is applied to a composite plate and that the neutral plane is located at z=0. The top surface is at $z=h_2$ and the bottom surface is at $z=-h_1$. The elastic strain, ε, resulting from this applied curvature is thus given by

$$\varepsilon = -Kz, \tag{A.1}$$

where K is a uniform curvature and z is the z-coordinate. The resulting stress is given by

$$\sigma = -\frac{E^{(k)}}{1-\upsilon^{(k)}}Kz, \tag{A.2}$$

where $E^{(k)}/1-\upsilon^{(k)}$ is the biaxial modulus of the kth layer. In order to maintain a force balance, the total force in the plate must equal to zero. Therefore,

$$\int_{-h_1}^{h_2}\sigma dz = 0. \tag{A.3}$$

The location of the neutral plane must satisfy equation (A.3), which is simplified as

$$\sum_{k=1}^{n}\frac{E^{(k)}}{1-\upsilon^{(k)}}\frac{1}{2}\left(h^{(k+1)^2} - h^{(k)^2}\right) = 0, \tag{A.4}$$

where $h^{(k)}$ is the z-coordinate of the bottom surface of the kth layer. Using the same notation adopted in Chapter 2, equation (A.4) is turned into a more familiar form as

$$B_{11} + B_{12} = 0, \tag{A.5}$$

which is a condition the location of the neutral plane must satisfy.

Appendix B

Strain of a Composite Beam

The dimensions of a homogeneous, stress-free beam changes when a film, with a residual stress σ_f, is deposited on all the surfaces of the beam. The change in length, Δ, results in a strain in the beam that is given by

$$\varepsilon = \Delta/\ell, \tag{B.1}$$

where ℓ is the length of the beam. The stress of the beam, σ_s, resulting from this strain, is then given by

$$\sigma_s = E_s\varepsilon, \tag{B.2}$$

where E_s is the Young's modulus of the beam. Correspondingly, the stress of the film, σ_f', is then

$$\sigma_f' = \sigma_f - E_f\varepsilon, \tag{B.3}$$

where E_f is the Young's modulus of the film. To maintain a force balance, the total force of the composite beam in the length direction must equal zero. Ignoring the film deposited on the sidewalls and the corners of the beam, we have

$$\sigma_s h_s + 2\sigma_f h_f = 0, \tag{B.4}$$

where h_s is the thickness of the beam and h_f is the thickness of the film. Substituting equations (B.2) and (B.3) into equation (B.4), we have the following expression for the stress of the film as measured by the dimensional change of the beam:

$$\sigma_f = \left(E_s h_s + 2E_f h_f\right)\frac{\Delta}{\ell}, \tag{B.5}$$

which, if expressed in terms of the stress-thickness product, becomes

$$\sigma_f h_f = \left(\frac{h_s}{2h_f}E_s + E_f\right)\frac{\Delta}{\ell}. \tag{B.6}$$

References

[Abe 90]   R. Abermann, "Measurements of the Intrinsic Stress in Thin Metal Films," *Vacuum* **41**, 1279 (1990).

[Ben 95]   M.S. Benrakkad, M.A. Benitez, J. Esteve, J.M. López-Villegas, J. Samitier, and J.R. Morante, "Stress Measurement by MicroRaman Spectroscopy of Polycrystalline Silicon Structures," *J. Micromech. Microeng.* **5**, 132 (1995).

[Bla 98]   A.R. Blanchet, *Microelectromechanical (MEMS) Structures for Thin Film Property Measurement*, S.M. Thesis, Massachusetts Institute of Technology (1998).

[Ble 82]   I. Blech and U. Cohen, "Effects of Humidity on Stress in Thin Silicon Dioxide Films," *J. Appl. Phys.* **53**, 4202 (1982).

[Bog 96]   A.E. Bogdanovich and C.M. Pastore, *Mechanics of Textile and Laminated Composites*, Chapman & Hall, London, UK (1996).

[Chi 80]   C.Y. Chia, *Nonlinear Analysis of Plates*, McGraw-Hill, New York (1980).

[Dri 93]   B.P. van Drieënhuizen, J.F.L. Goosen, P.J. French, and R.F. Wolffenbuttel, "Comparison of Techniques for Measuring Both Compressive and Tensile Stress in Thin Films," *Sensors Actuators A* **37-38**, 756 (1993).

[Elb 97]   L. Elbrecht, U. Storm, R. Catanescu, and J. Binder, "Comparison of Stress Measurement Techniques in Surface Micromachining," *J. Micromech. Microeng.* **7**, 151 (1997).

[Eri 95]   F. Ericson, S. Greek, J. Söderkvist, and J.Å. Schweitz, "High Sensitive Internal Film Stress Measurement by An Improved Micromachined

Indicator Structure," *IEEE 8th International Conference on Solid-State Sensors and Actuators*, 84 (1995).

[Fan 94]   W. Fang and J.A. Wickert, "Post Buckling of Micromachined Beams," *J. Micromech. Microeng.* **4**, 116 (1994).

[Flo 97]   J.A. Floro, E. Chason, S.R. Lee, R.D. Twesten, R.Q. Hwang, and L.B. Freund, "Real-Time Stress Evolution During $Si_{1-x}Ge_x$ Heteroepitaxy: Dislocations, Islanding, and Segregation," *J. Electron. Mater.* **26**, 969 (1997).

[Gia 96]   Y.B. Gianchandani and K. Najafi, "Bent-Beam Strain Sensors," *J. Microelectromech. Syst.* **5**, 52 (1996).

[Glo 95]   D.A. Glocker and S.I. Shah, *Handbook of Thin Film Process Technology*, IOP Publishing, Bristol, UK (1995).

[Guc 85]   H. Guckel, T. Randazzo, and D.W. Burns, "A Simple Technique for the Determination of Mechanical Strain in Thin Films with Applications to Polysilicon," *J. Appl. Phys.* **57**, 1671 (1985).

[Guc 92]   H. Guckel, D. Burns, C. Rutigliano, E. Lovell, and B. Choi, "Diagnostic Microstructures for the Measurement of Intrinsic Strain in Thin Films," *J. Micromech. Microeng.* **2**, 86 (1992).

[Jen 88]   D.W. Jensen and P.A. Lagace, "Influence of Mechanical Couplings on the Buckling and Postbuckling of Anisotropic Plates," *AIAA J.* **26**, 1269 (1988).

[Kim 99]   Y.S. Kim and S.C. Shin, "Layer-by-Layer In Situ Stress Measurements of Metallic Multilayers with Atomic-Layer Sensitivity," *J. Magn. Magn. Mater.* **198-199**, 602 (1999).

[Klo 68]   E. Klokholm and B.S. Berry, "Intrinsic Stress in Evaporated Metal Films," *J. Electrochem. Soc.* **115**, 823 (1968).

[Kob 00]   M.J. Kobrinsky, E.R. Deutsch, and S.D. Senturia, "Effect of Support Compliance and Residual Stress on the Shape of Doubly-Supported Surface-Micromachined Beams," accepted for publication in *J. Microelectromech. Syst.* (2000).

[Kob₂ 00]   M.J. Kobrinsky and C.V. Thompson, "Activation Volume for Inelastic Deformation in Polycrystalline Ag Thin Films," *Act. Mat.* **48**, 625 (February 2000).

[Kus 96]   K. Kusaka, T. Hanabusa, M. Nishida, and F. Inoko, "Residual Stress and In-Situ Thermal Stress Measurement of Aluminum Film Deposited on Silicon Wafer," *Thin Solid Films* **290-291**, 248 (1996).

[Kus 98]   W.M. Kuschke, A. Kretschmann, R.M. Keller, R.P. Vinci, C. Kaufmann, and E. Arzt, "Textures of Thin Copper Films," *J. Mater. Res.* **13**, 2962 (1998).

[Lin 97]   L. Lin, A.P. Pisano, and R. Howe, "A Micro Strain Gauge with Mechanical Amplifier," *J. Microelectromech. Syst.* **6**, 313 (1997).

[Mas 88]   F. Maseeh, M.A. Schmidt, M.G. Allen, and S.D. Senturia, "Calibrated Measurements of Elastic Limit, Modulus, and the Residual Stress of Thin Films Using Micromachined Suspended Structures," ," *IEEE Solid-State Sensor and Actuator Workshop*, 84 (1988)

[Meh 87]   M. Mehregany, R.T. Howe, and S.D. Senturia, "Novel Microstructures for the In Situ Measurement of Mechanical Properties of Thin Films," *J. Appl. Phys.* **62**, 3579 (1987).

[Nes 99]   D.C. Nesting, J. Kouvetakis, S. Hearne, E. Chason, and I.S.T. Tsong, "Real-Time Monitoring of Structure and Stress Evolution of Boron Films Grown on Si(100) by Ultrahigh Vacuum Chemical Vapor Deposition," *J. Vac. Sci. Technol. A* **17**, 891 (1999).

[Nic 99]   L. Nicu, P. Temple-Boyer, C. Bergaud, E. Scheid, and A. Martinez, "Energy Study of Buckled Micromachined Beams for Thin-Film Stress Measurements Applied to SiO_2," *J. Micromech. Microeng.* **9**, 414 (1999).

[Ohr 92]   M. Ohring, *The Materials Science of Thin Films*, Academic Press, Boston, Massachusetts (1992).

[Ost 97]   P.M. Osterberg and S.D. Senturia, "M-Test: A Test Chip for MEMS Material Property Measurement Using Electrostatically Actuated Test Structures," *J. Microelectromech. Syst.* **6**, 107 (1997).

[Pan 99]   C.S. Pan and W. Hsu, "A Microstructure for *In Situ* Determination of Residual Strain," *J. of Microelectromech. Syst.* **8**, 200 (1999).

[Pop 94]   D.S. Popescu, T.S.J. Lammerink, and M. Elwenspoek, "Buckled Membranes for Microstructures," *Proc. IEEE Micro. Electro. Mech. Syst., Osio, Japan*, 188 (1994).

[Qat 93]   M.S. Qatu and A.W. Leissa, "Buckling or Transverse Deflections of Unsymmetrically Laminated Plates Subjected to In-Plane Loads," *AIAA J.* **31**, 189 (1993).

[Sam 92]   J. Samitier, S. Marco, O. Ruiz, J.R. Morante, J. Esteve-Tinto, and J. Bausells, "Analysis by FT-IR Spectroscopy of SiO_2-Polycrystalline Structures Used in Micromechanics: Stress Measurements," *Sensors Actuators A* **32**, 347 (1992).

[Sch 92]   J.A. Schweitz, "Mechanical Characterization of Thin Films by Micromechanical Techniques," *MRS Bull.* **17**, 34 (1992).

[Sri 99]   V.T. Srikar, unpublished results (1999).

[Tencor]   *Tencor FLX-2320 Thin Film Stress Measurement User Manual*

[Tho 93]   C.V. Thompson, "The Origin of Epitaxial Orientations in Thin Films," *Mat. Res. Soc. Symp. Proc.* **280**, 307 (1993).

[Tim 36]   S. Timoshenko, *Theory of Elastic Stability*, McGraw-Hill, New York (1936).

[Tsa 88]   S. Tsai, *Composites Design, 4th Ed.*, Think Composites, Dayton, Ohio (1988).

[Vla 92]   J.J. Vlassak and W.D. Nix, "A New Bulge Test Technique for the Determination of Young's Modulus and Poisson's Ratio of Thin Films," *J. Mater. Res.* **7**, 3242 (1992).

[Whi 87]   J.M. Whitney, *Structural Analysis of Laminated Anisotropic Plates*, Technomic, Lancaster, Pennsylvania (1987).

[Wil 92]   L.B. Wilner, "Strain and Strain Relief in Highly Doped Silicon," *IEEE Solid-State Sensor and Actuator Workshop*, 76 (1992).

[Win 00]   D.L. Windt, "Stress, Microstructure, and Stability of Mo/Si, W/Si, and Mo/C Multilayer Films," *J. Vac. Sci. Technol. A* **18**, 980 (May-June 2000)

[Zie 99]   V. Ziebart, O. Paul, and H. Baltes, "Strongly Buckled Square Micromachined Membranes," *J. Microelectromech. Syst.* **8**, 423 (1999).